OPAL SILICON MICROVERTEX DETECTOR

OPAL COLLABORATION

TECHNICAL PROPOSAL

JANUARY 1990

Contents

1 Introduction

This proposal describes a silicon strip microvertex detector that will provide the most precise information at the centre of the OPAL tracking system. The detector, together with a new beam-pipe of reduced radius, will be installed during the major LEP shutdown of 1990-91. Each of the two silicon layers, shown in fig. 1, will provide measurements of high spatial precision ($\sim 5 - 10\mu m$) in two orthogonal co-ordinates at radii close to the interaction region, and have an excellent two-particle resolution $\sim 150\mu m$.

In Section 2 we address the physics objectives of the microvertex detector and summarise the most important results derived from including it within the GOPAL Monte Carlo simulation of OPAL. Technical details of the simulation and a full review of the quantitative conclusions are given in Appendix A. Appendix B contains a note on a method for finding secondary vertices using the silicon digitisings for the decay products of short-lived states such as B and D hadrons.

Section 3 gives the proposed geometry of the complete detector as well as a survey of the electronics and the associated readout scheme. The method of installation within the existing OPAL central region is also explained. Section 4 outlines the timetable for the project. Summary and conclusions are presented in Section 5.

2 Study of the Physics Potential of the OPAL Microvertex Detector

It is now well accepted[1] that silicon-based tracking detectors will play an important role in the experiments at LEP as we move to the era of high luminosity running at the Z° peak and in subsequent years to even higher event rates with multi-bunch operation.

Silicon microstrip detectors have already been installed, around the existing 8cm radius beam-pipes, by ALEPH[2] and DELPHI[3]. We have benefitted much from their knowledge and this has been a vital ingredient in allowing us to formulate the present OPAL proposal.

The physics aims of the OPAL Microvertex Detector relate specifically to its ability to localise interactions with a precision high enough to allow some separation of primary and secondary vertices on an event by event basis. This will provide, for the first time, efficient tagging of short-lived particles and allow precise measurements of their lifetime down to the level of 10^{-13}sec. Such tagging is particularly important in the area of B physics and of course for any new phenomena at LEP energies which produce particles with millimetre decay paths. With about one quarter of all Z° decays containing pairs of either charm or bottom quarks as their fragmentation source, an integrated luminosity of 50pb^{-1} will provide about 300K $b\bar{b}$ pairs. A recent detailed account of heavy flavour physics at LEP has been produced from the 1989 Workshop on Z Physics at LEP [4].

Currently in OPAL the quality of the vertex reconstruction is controlled by the drift

3

chamber digitisings from the chamber that immediately surrounds the existing 8cm radius beam-pipe. This chamber is achieving $(r - \phi)$ precisions close to 50 microns per point, which are reasonably matched to the limitations arising for low momentum tracks from the combined effects of multiple scattering in the beam-pipe and the extrapolation lever arm back to the vertex. However, the proposed reduction in beam-pipe radius, down to between 5 and 6cm, will make it possible to reduce the net lever arm by inserting the two layers of silicon strip detector. It is then also important to have the very good precision and two-particle resolution characteristic of a silicon detector.

We have considered several detector configurations ranging from one layer of single sided wafers through to two layers of double sided devices. It is the latter system that we propose to construct in order to give two precise co-ordinates per track in both $(r - \phi)$ and $(r - z)$ using detectors with orthogonal sets of strips built onto their opposite faces.

The results of a comprehensive study of Monte Carlo simulations are given in Appendix A. A measure of the improvement in distinguishing primary and secondary vertices is found in the impact parameter resolution, which can be investigated with isolated muon tracks. In appendix A, fig. 2 shows that the proposed silicon detectors improve the impact parameter in the $(r - \phi)$ plane by a factor of 2 at low momenta, and by up to a factor 4 at higher energies where the effects of multiple scattering are small. Figure 4 shows the same parameter in the $(r - z)$ plane where the improvement compared with existing OPAL is even more dramatic, amounting to a factor of 8 or more at all energies. Figure 6 demonstrates that the silicon co-ordinates can be clearly associated with the correct tracks, as provided by the neighbouring drift chambers. This efficient pattern recognition arises from the radial nature of even low momentum tracks so that ϕ-angle cuts link together the appropriate co-ordinates from the inner and outer silicon layers.

The studies have been done for various beam-pipe radii and detector arrangements. The results indicate that all the feasible implementations within OPAL would give similar enhancements. Clearly the closer the inner layer of detectors can be placed to the interaction point the greater is the improvement on the impact parameter resolution.

We have also investigated vertex-finding, using reconstructed tracks to distinguish between particles coming from the primary interaction point and those from secondary decays. A preliminary study is reported in appendix B, where the silicon detector is shown to make significant improvements in both purity and efficiency for reconstruction of vertices from both B and D decays. As an illustration, values of 32% and 10% for purity and efficiency of secondary vertex finding in the present OPAL drift chamber system are improved by nearly a factor of 3, to 86% and 30%, with the addition of the new silicon detectors.

The simulation of event reconstruction and the study of b-tagging and specific physics decay channels is a continuing process. A preliminary study[5] has considered some typical exclusive decays of B or charmed hadrons:

4

$$B \to D^{\circ} \pi^+ \pi^- \pi^-, \text{ where } D^{\circ} \to K \pi^+, \ D^{\circ} \to K^- \pi^+ \pi^- \pi^+,$$

$$D^{\circ} \to K^- \pi^+$$

$$\text{and } D^{\circ} \to K^- \pi^+ \pi^- \pi^+$$

The results indicate the importance of providing two orthogonal space measurements in each of the silicon layers, when an order of magnitude improvement in the signal to noise ratio for exclusive B decays may be achieved. Such considerations lead to the need for double-sided devices as we propose in the following technical specification. We believe the investigations we have carried out so far demonstrate that the proposed silicon tracking system will provide a further powerful tool for physics in OPAL.

3 The OPAL Silicon Microvertex Detector

3.1 The beam-pipe

At present a high precision drift chamber forms the innermost element of the OPAL central tracking system and immediately surrounds the 8cm radius beam-pipe. Based on experience gained in the initial LEP runs in 1989 we now expect to install in the next long shutdown a new inner beam-pipe with reduced radius, perhaps as small as 5cm, without risk of seriously increasing the level of background radiation. The proposed silicon detector will fit within the annulus between the new beam-pipe and the existing tracking system.

Initially we considered installing the silicon detector inside the gas volume of the present OPAL central detector in order to maximise the benefit from the extra radial space. However, practical considerations and a wish to minimise the amount of material between the interaction point and the silicon layers have led to the present scheme. Here the silicon detector is installed between a new LEP beam-pipe of smaller radius and a replacement of the present pipe closing off the central detector pressure vessel at its inner radius. A major advantage of this scheme is that it maintains the integrity of the existing gas detector volume. Once the new pipe has been installed the microvertex detector can be accessed for completion or repair without jeopardising the existing OPAL tracking system and within a relatively short shut-down period of $\sim$3-4 weeks.

The new beam-pipe will be of similar structure to the central section of the present one, consisting of a thin aluminium inner cylinder 0.1mm thick around which carbon fibre is wound to a thickness of 1.2mm. A total pipe length of 6m is produced by welding together 1m units each of which has 1.5mm thick aluminium end flanges. The existing OPAL beam-pipe, which forms the inner surface of the central detector pressure vessel, will be replaced by a new smooth 2mm thick carbon fibre tube. This will be made in one piece, without aluminium lining, and its flanges will be located outside the angular acceptances of the central detector and of the forward detector.

3.2 The Silicon Strip Detectors

Experience has recently been gained in the use of single-sided capacitively coupled silicon microstrip devices in the DELPHI experiment at LEP. In addition, both ALEPH[6] and DELPHI[7] have recently reported the successful operation of double-sided devices in test beam runs at CERN. These should provide important results on, for example, the radiation stability of biasing circuits, and the space resolution in both co-ordinates and its dependence on incident angle and detector readout spacing. Already the ALEPH detector at LEP incorporates some double-sided devices and DELPHI plans to add them within the next year.

Advances continue to be made in detector fabrication. Devices, typically 300μm thick, with strip pitches down to 25μm on the diode side achieve spatial resolutions of $\sim$ 5μm from readout every 50μm. The DELPHI group[8] first demonstrated the use of capacitive coupling to the readout strips, removing the sensitivity to variations in leakage current. They also pioneered the use of polysilicon to provide biasing of all strips, and so achieve interstrip capacitive charge division, a tool for gaining improved resolution.

Both ALEPH[2] and DELPHI[7] have made important contributions to the development of double-sided devices. The strip pitch on the reverse (ohmic) side is presently 50 to 100μm, and the current designs incorporate techniques of either field induced junction isolation[7] or p-implant compensation[2].

The devices to be installed in OPAL will clearly benefit much from this earlier work. We envisage our basic elements to be double-sided devices with dimensions close to 60mm by 33mm. These will be mounted into modules containing 3 elements connected serially. We are also investigating the use of thin (150–200μm) single-sided detectors positioned back to back, with orthogonal strips, as a solution if all the final detectors are not available during 1990. The double-sided option is preferred as representing slightly less total material, giving a larger signal and so making less exacting demands on the read out electronics, and allowing the use of Landau correlations. It should be noted, however, that our pattern recognition studies have assumed uncorrelated silicon $(r - \phi)$ and $(r - z)$ track coordinates. The $(r - \phi)$ strips will have a pitch of 25μm, with readout of alternative strips. In $(r - z)$ most tracks are inclined to the detector, and here the readout pitch will be 100μm.

3.3 The Geometrical Layout

The two layers of detector modules will be arranged as shown in fig. 1. The present layout is shown for the worst case of a beam pipe of 6cm radius, when there is insufficient space to arrange overlap between successive modules in the $(r - \phi)$ projection. However, this design has complete azimuthal coverage for one digitizing per track and 80–90% of the solid angle is covered by active elements in both layers. Along the z-direction there are negligible dead areas within the acceptance limits $-0.76 < \cos\theta < 0.76$. With an annular space of 17mm for the whole detector the lever arm between the two layers is typically 8mm.

The detector will be constructed in two separate half-cylinder shells that will be assembled

together in-situ around the beam-pipe. The complete assembly will be supported within the 2mm thick carbon fibre tube that forms the inner wall of the central detector pressure vessel.

Each half shell contains two layers of detector modules, shown in section in fig. 2. A ladder module is shown in fig. 3 and consists of 3 connected elements each of width 33mm and with a total length of about 180mm. This provides polar angle coverage from 40° to 140°.

The outer layer in a half shell contains 7 modules, and the inner has 6 for a beam-pipe of 6cm radius. If this radius were reduced as far as 5cm the inner layer would need only 5 modules. Alternatively, a construction with overlapping modules within a layer could be considered. The three double-sided silicon detectors forming each module are mounted on a thin printed circuit support that also provides the interconnections for the z-strip readout. This allows the VLSI amplifier-multiplexers (Microplex) to be mounted at the end of the detector chain, and out of the path of particles traversing the active area of any detector element, in a similar position to those reading out the $(r - \phi)$ information from the opposite surface (see fig. 3). Mounting electronics only at one end of each module simplifies both the design and the cooling.

The specific dimensions of the OPAL detectors allow them to be fabricated from 3″ diameter silicon wafers and are compatible with the 6.4mm wide Microplex chip.

3.4 Readout Scheme

A schematic of the readout elements associated with one layer of the complete detector is shown in fig. 4. This illustrates our goal of accessing the data from one module end only, from which power, control and cooling are also serviced. Fig. 5 gives more detail of the electronics that will be mounted on the detector ladder module. The readout of each plane of co-ordinates for a module will require five Microplex chips[9], each with 128 channels, controlled by a local sequencer with its associated calibration unit. A development of the MX3 microplex, MX5, with improved performance specification, is now being processed for use in OPAL. Line drivers and receivers will be mounted on a separate support interconnect-ring with connections to the detector modules being made through thin flexible strips. Driving electronics, digitizers (Sirocco IV [10]) and power supplies will be in an electronics hut.

This scheme assumes that three silicon detectors are daisy chained in $(r - \phi)$ giving a total of 640 readout channels per module. Similarly the z strips will be interconnected between the three sub-elements such that the ith channel of each one becomes serialised (fig. 5). This leads, in principle, to a three-fold ambiguity in the $(r - z)$ track position, but Monte Carlo simulations have shown that it is straightforward to remove this within the overall OPAL track reconstruction. The daisy chaining is done with three sets of pcbs which are glued on the back of the ladder support, the z strips being bonded at both ends to these pcbs. The readout pitch is chosen to match the 640 channels provided by five microplexes on the end-support.

7

3.5 Cooling

The cooling is done by means of water channels embedded into the half ring supports of the microvertex detector assembly. The arrangement is illustrated in fig. 6. The efficient heat transfer to the cooling circuit is achieved by having direct mechanical contact between the aluminium support and the end structure of each detector module where the VLSI electronics is mounted. Temperatures will be monitored by sensors placed on the modules.

Simulations have shown that temperature differences can be kept below 2°C. The water will be supplied from the 20°C stabilised cooling circuit that already exists for OPAL. Fine temperature regulation will ensure that minimum perturbations are caused to the surrounding sub-detectors.

3.6 Survey

Calibration and alignment of individual silicon wafers within modules will be carried out during assembly in the laboratory. In beam tests precision telescopes of silicon detectors will allow track positions to be known, so that the dependence of measured co-ordinates on hit position and incident track angle can be determined. Both modules and the complete detector will be measured in a test beam, as well as in the laboratory, in order to determine their geometry with the best possible precision before installation.

The whole assembly will sit within the carbon fibre cylinder that closes the central detector pressure vessel. This cylinder is attached to the end cones of the central drift chamber. Stable positioning will be maintained by tight temperature control and low gradients, with the final survey relying on fitted tracks.

4 The Project Timetable

4.1 The Silicon Microstrip Detectors

Handling and testing facilities are now being set up for double-sided detectors. OPAL prototype devices will be available in summer 1990, with the supply of final detectors beginning in autumn 1990.

Prototype single-sided detectors are now available for testing back-to-back assemblies. Tests will continue until summer 1990. OPAL prototypes will be available during early summer 1990.

4.2 Electronics

Microplexes (MX5) are now being processed and will be available from April 1990. The electronics directly attached to the detector module and in the interconnect region is now under design.

The digitising modules and power supplies are available commercially.

4.3 Beam-pipe and Mechanical Supports

The new beam-pipe will be provided by the LEP Division and should be available when required for installation. All the associated handling equipment for installation has been designed.

Design of the detector mechanical supports is well advanced and prototype pieces are about to be made. The fabrication will be complete during summer 1990.

4.4 Beam Tests

Arrangements and necessary facilities for beam tests during the second half of 1990 are being made.

5 Summary and Conclusions

In this proposal we have outlined the impact that can be expected from adding a Silicon Strip Microvertex Detector at the centre of the OPAL experiment. The project is challenging in both its demands on instrumentation techniques and in its necessary timescales.

The construction, testing, installation and commissioning of the system have been carefully evaluated, to ensure that it can be smoothly integrated into the central tracking of OPAL.

The successful implementation of the proposed detector will add a new and powerful feature to the physics studies of the OPAL experiment at LEP.

References

[1] Minutes of the 16th LEPC meeting; CERN/LEPC 87-8.

[2] P. Holl et al., "The ALEPH Minivertex Detector" Nucl. Instr. and Meth. A257, 587 (1987). P. Holl et al., "A Double Sided Silicon Strip Detector with Capacitive Readout and a New Method of Integrated Bias Coupling", IEEE Trans. on Nucl. Sci., Vol. 36, No. 1, 1988, p.251.

[3] DELPHI Microvertex Detector, addendum to the Technical Proposal, DELPHI 86-86 GEN-2 (Oct. 1986). G. Anzivino et al., Nucl. Instr. and Meth. A263 215 (1988).

[4] "Z Physics at LEP 1", Vol. 1, CERN 89-08 edited by G. Altarelli, R. Kleiss and C. Verzegnassi.

[5] "A study of some physics aspects of a Microvertex Detector in OPAL", A. Jawahery, 27/SILICON-0001.

[6] ALEPH Microvertex Group, private communication.

[7] "A New Microstrip Detector with Double-Sided Readout", B.S. Avset et al., paper presented by P. Weilhammer at 1989 IEEE Nucl. Science Symposium, San Fransico Jan. 1990.

[8] M. Caccia et al., Nucl. Instr. and Meth. 260 124 (1987).

[9] "A low power CMOS VLSI multiplexed amplifier for silicon strip detectors", P.P. Allport et al., RAL-87-079 (1987).

[10] "SIROCCO—A Silicon Strip Read-Out CAMAC Controller", A. Lang and J.P. Vanuxem CERN-EP Electronics Note 86-01, also developed to SIROCCO IV (Fastbus) by N. Bingefors and M. Burns.
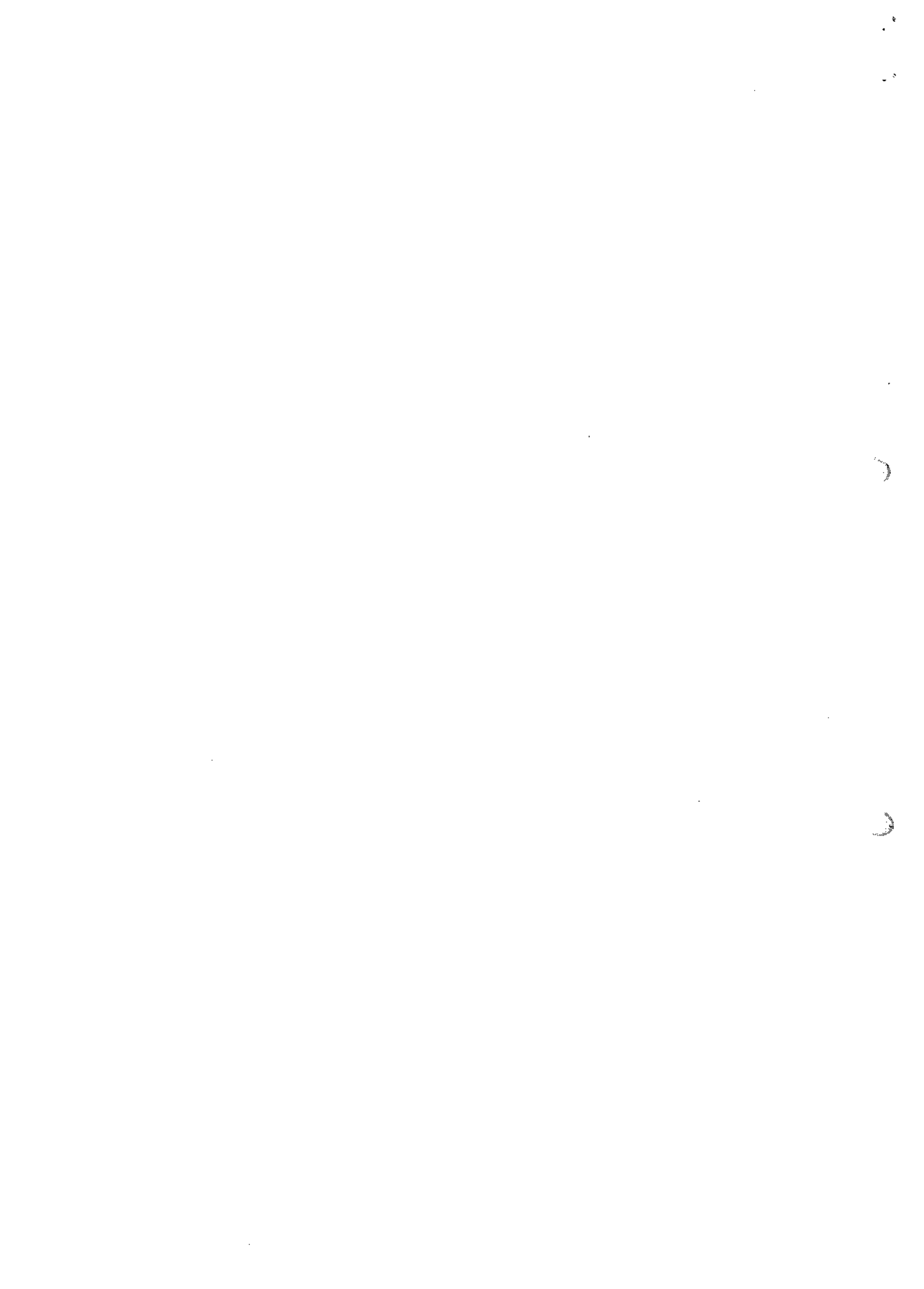
Figure Captions

Fig. 1: The layout in the $(r - \phi)$ plane of two layers of silicon strip detectors bounded by an inner beam-pipe of 60mm radius and an outer tube of 80mm radius.

Fig. 2: Details of a quadrant of detectors, as in fig. 1, showing the support profiles for each module.

Fig. 3: A ladder module of detectors showing the electronics and cooling that is on-board the support frame.

    (a) plan view of $(r - \phi)$ detector side,

    (b) side view showing the modules in the inner, and outer layers together with the water cooling circuits at the ends,

    (c) plan view of $(r - z)$ detector side showing the daisy chaining between wafers.

Fig. 4: A schematic of the readout for one layer of detector modules indicating the elements of the system.

Fig. 5: The local ladder electronics for a module of detectors.

Fig. 6: Cross-section of support ring showing the cooling circuits and aluminium heat conduction structure.

Figure 1

Figure 2

(a) (b) (c)

Figure 3

Interconnect
Ring

Buffer
Electronics

Bulkhead
Connection

Power
Supply

Silicon
Control
Unit

DAQ
Sirocco
IV

Opal Silicon
Microvertex Detector
SCHEMATIC of one Layer

Figure 4

μPX : MICROPLEX MX5
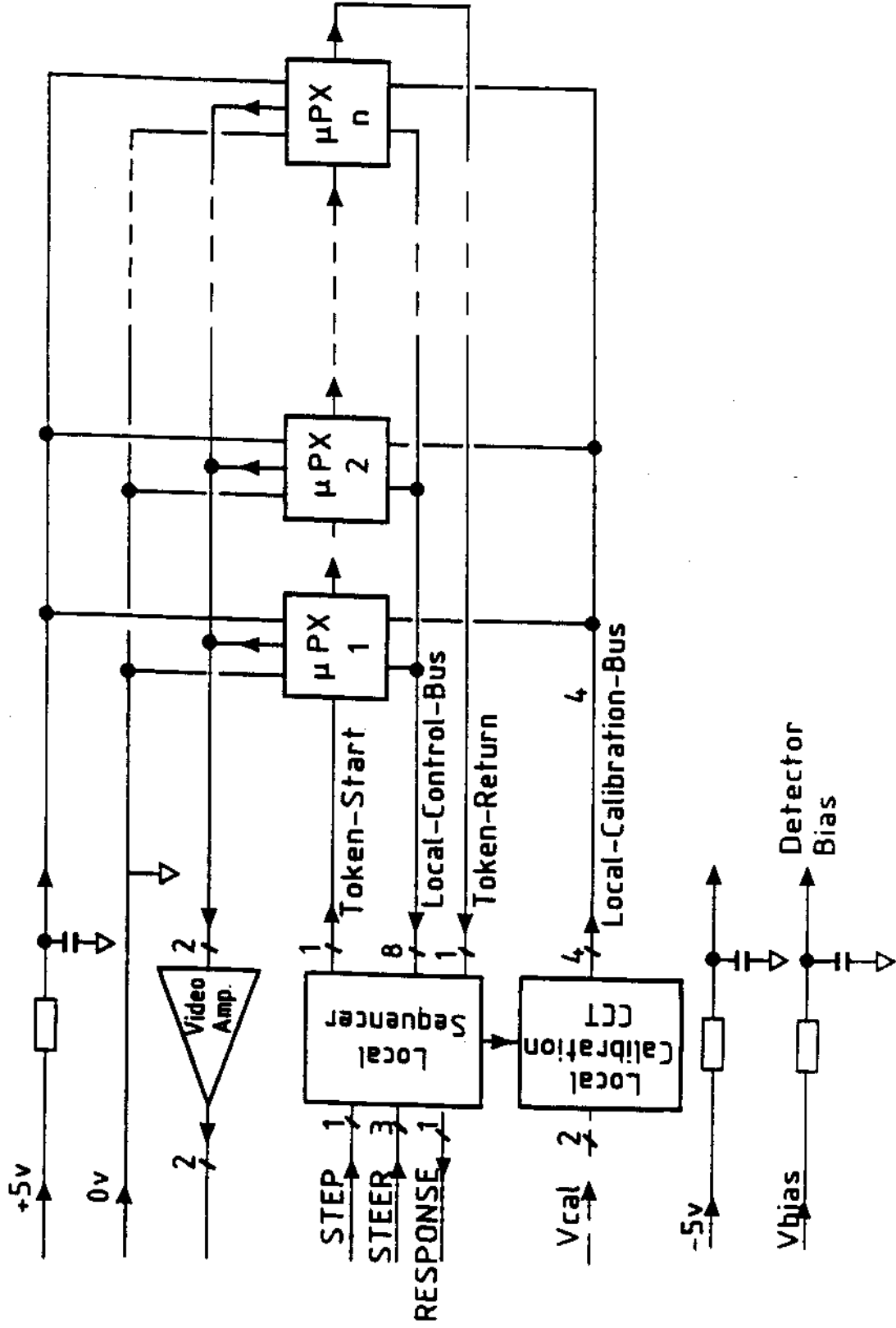
LOCAL LADDER ELECTRONICS
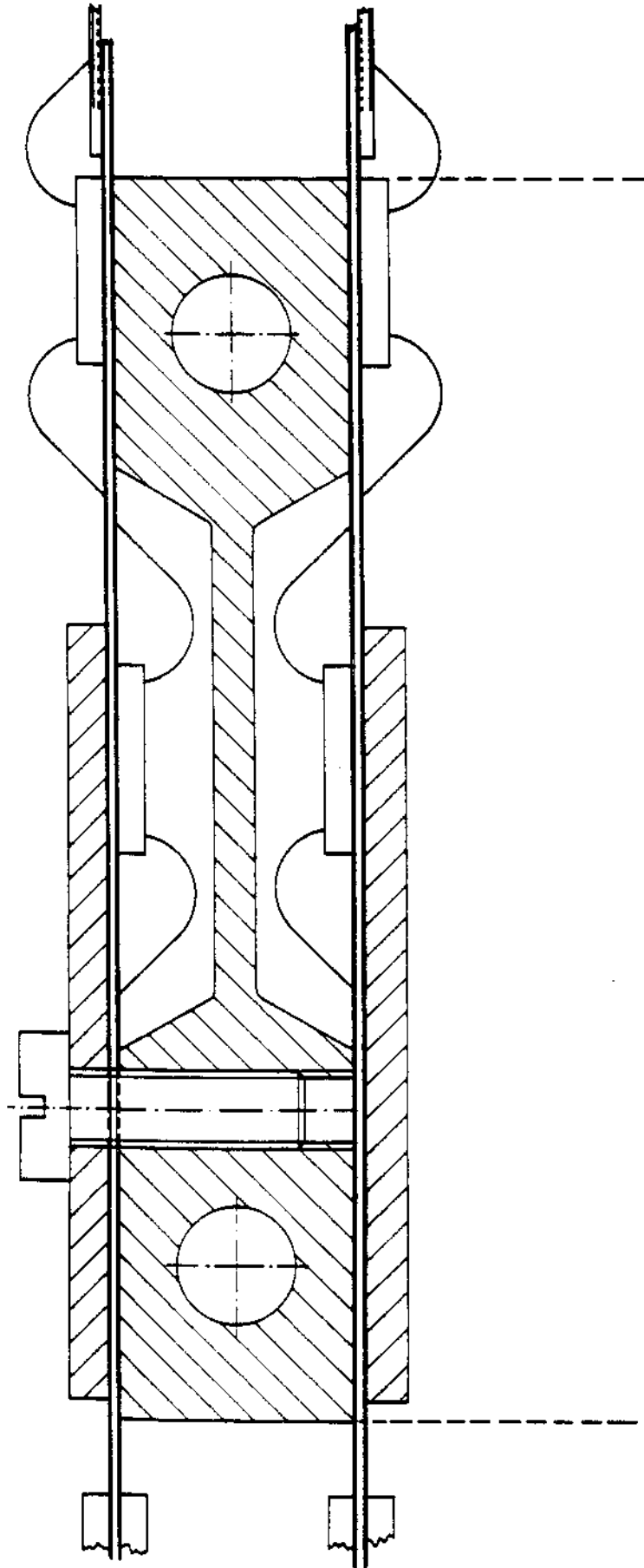
Figure 6

Simulation Studies of a Silicon Microvertex Detector for OPAL

J R Batley and D R Ward

October 1989

Abstract

The results of Monte Carlo simulation studies of the addition of a silicon microvertex detector are described. The improvement in charged track reconstruction (especially impact parameter resolution) that would be provided by such a detector is studied as a function of the detector parameters. Pattern recognition with a silicon detector is considered for both one-sided and two-sided detectors. The position resolution for reconstructed primary and secondary (B and D decay) vertices in $B\bar{B}$ events is compared with and without a silicon microvertex detector. Indications as to the improvement in B-tagging with silicon are presented.

1 Introduction

With a reduction in LEP beam pipe radius foreseen for 1991 [1], an attractive option for OPAL is to add a silicon microvertex detector inside the existing central detector. Such a detector would combine high spatial precision ($\sim 5\mu m$) with excellent two-particle separation ($\sim 150\mu m$) at a position close to the interaction point, thereby giving improved identification and reconstruction of the decays of short-lived particles such as B and D hadrons.
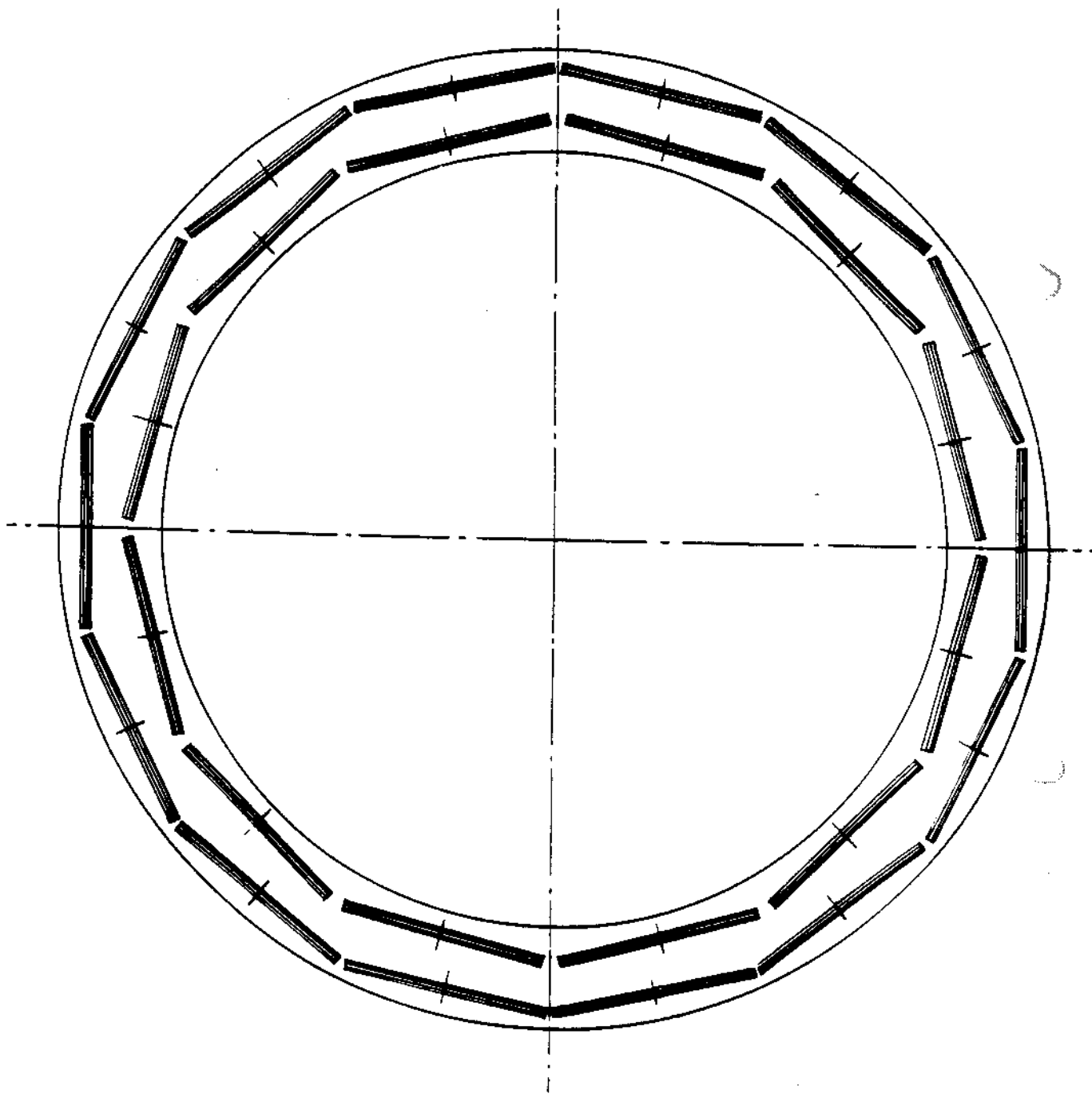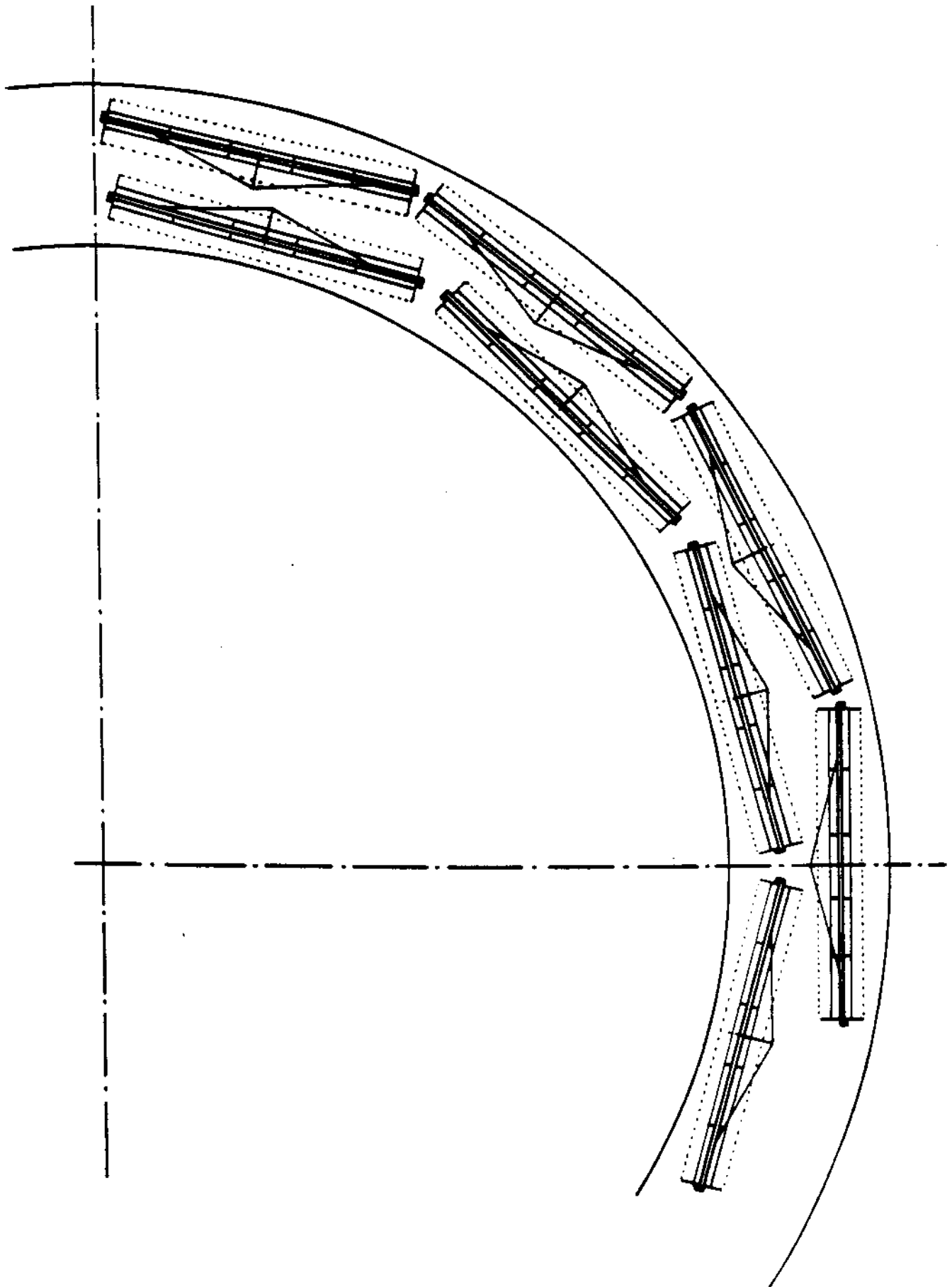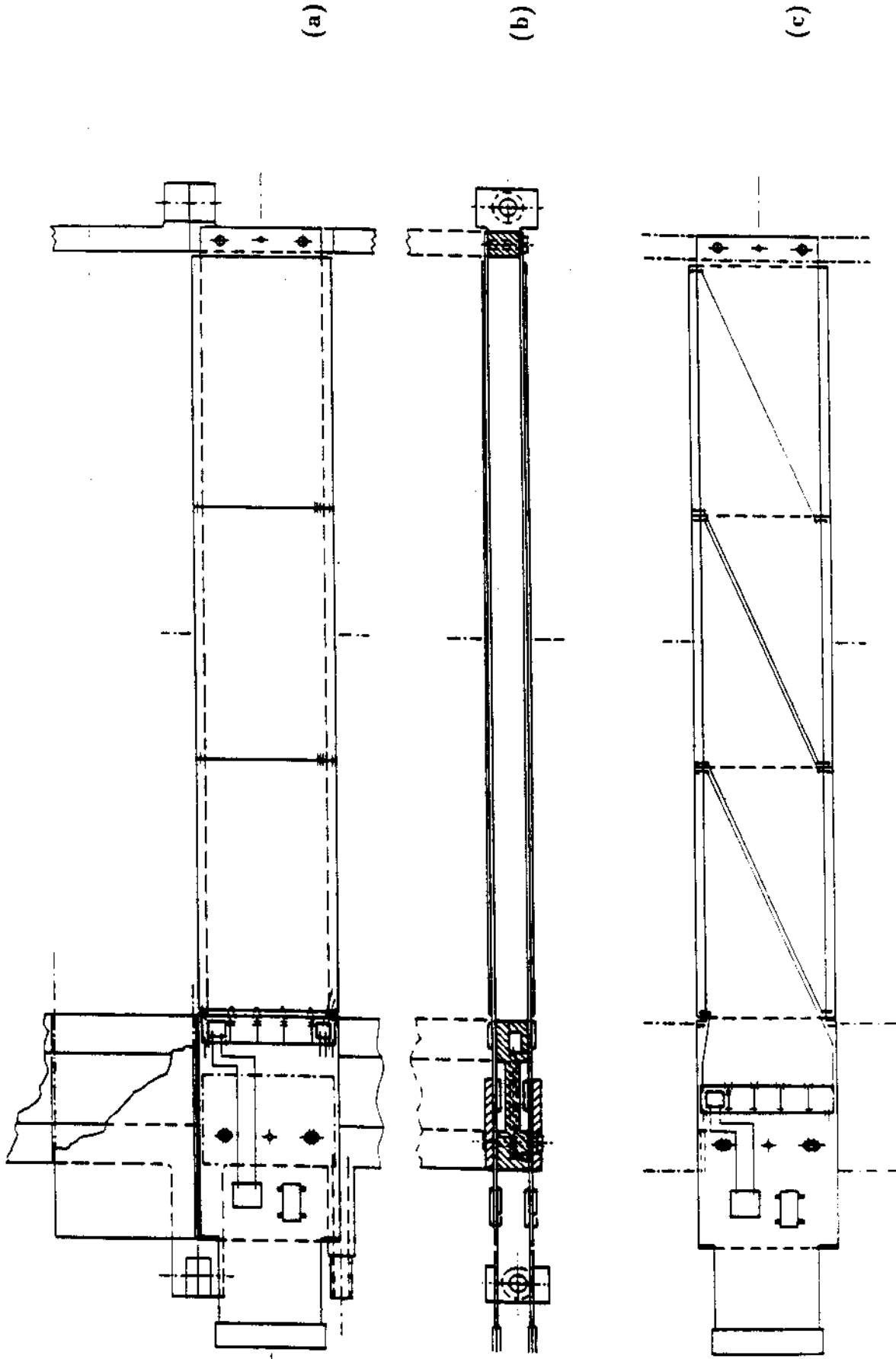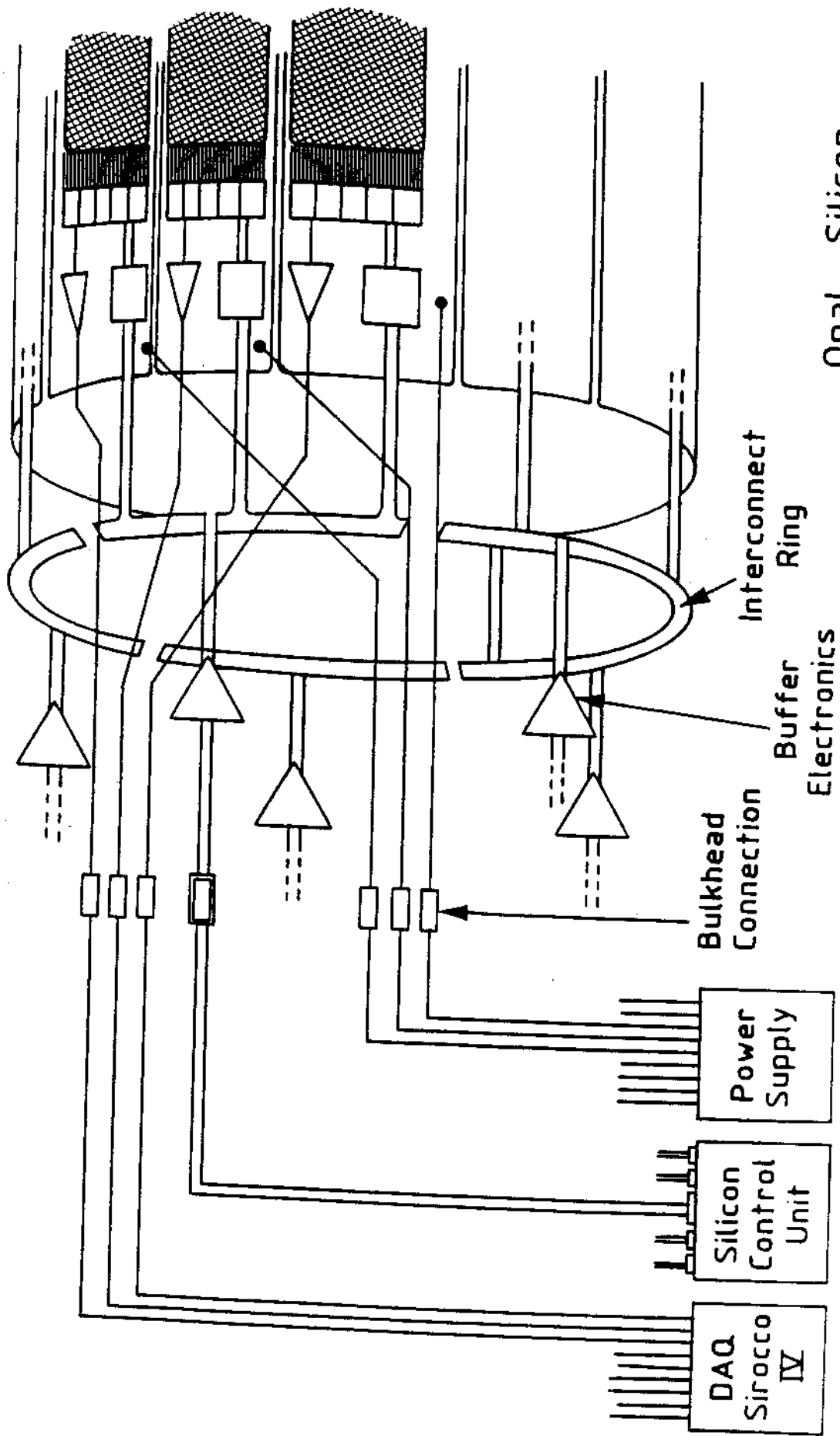
In this note, we describe the results of Monte Carlo (GOPAL) simulation studies of a silicon microvertex detector. The main aim of these studies is to quantify the improvement in track and vertex reconstruction which would result from the addition of a silicon vertex detector to OPAL, and to try to assess the physics benefits for the study of events containing short-lived particles, and especially for B physics studies.

Ideas for the possible design of a silicon detector have already been considered [2] [3]. The scheme outlined in reference [2] for example envisages a detector consisting of two barrels of silicon wafers with radii 6cm and 8cm sitting outside a beam-pipe of radius 5cm. A schematic view of this detector (from ref [2]) is shown in figure 1. The results described here will focus on this two barrel geometry, but we shall also consider other choices for the main silicon detector design parameters (number and radii of the silicon barrels, beam-pipe thickness and radius, silicon thickness etc.). In particular, the beam pipe radius may initially be reduced only to ~ 6cm and we shall consider possible one and two barrel detector geometries with this larger radius beam pipe [3].

We shall also compare the performance of "one-sided" and "two-sided" silicon detectors. For the simpler "one-sided" detector, with strips running along the z direction at constant azimuth, only the track position in the transverse (xy) view is available. For "two-sided" detectors, the z coordinate of the hit is also measured (with precision comparable to that for the xy hit) by reading out an orthogonal set of strips built onto the opposite face of the silicon wafers.

1

The overall plan of this document is as follows: in the next section we describe some technical aspects of the GOPAL simulation of the silicon detector and the subsequent analysis in ROPE. In section 3, we consider the improvement in resolution that a silicon detector would provide for the reconstruction of single charged tracks, especially the improvement in impact parameter resolution for both the transverse (xy) and the longitudinal (rz) projections. In section 4, we consider the problem of pattern recognition for the silicon detector, i.e. the problem of associating the silicon hits to the charged tracks reconstructed in the OPAL central detector (CV,CJ,CZ). Finally, in section 5, we study the improvement in precision on the positions of primary and secondary (B and D decay) vertices in $B\bar{B}$ events. We also try to assess the physics benefits of a silicon detector for secondary vertex identification and for the tagging of events containing short lived particles.

2   The Simulation Program

The simulation studies were carried out using the full simulation of the OPAL detector provided by GOPAL120 and GEANT313. The silicon detector was modelled using a simplified geometry consisting of two cylinders of silicon material placed at radii 6cm and 8cm. The thickness of each silicon cylinder was chosen to be $450\mu m$ to give the correct number of radiation lengths appropriate to a silicon wafer of thickness $300\mu m$ plus support material [2]. The total length of each cylinder was taken to be 40cm, giving a polar angle coverage for both silicon barrels to within $\theta=22°$ of the beam direction. In addition, the radius and thickness of the existing OPAL beam-pipe (0.13cm thickness of carbon fibre at a radius of 7.8cm) was reduced to 0.1cm thickness at a radius of 5.0 cm. The standard geometrical parameters used in the simulation are summarised in Table 1.

Table 1: Parameters used in GOPAL simulation.

Radius (cm)	Material	Thickness (cm)	Thickness (X_0)
5.0	C	0.1	0.46%
6.0	Si	0.0450	0.48%
8.0	Si	0.0450	0.48%

A uniform silicon spatial resolution in the transverse (xy) plane of $5\mu m$ was assumed; i.e. hits in the silicon detector were simulated by smearing the true charged track position with a Gaussian of width (rms) $5\mu m$. No allowance was made for a finite two track separation; a typical value for this for silicon microstrip detectors is $\sim150\mu m$. This is discussed further in the context of pattern recognition in section 4 below.

For the two-sided readout option whereby z information is also made available from the silicon by reading out orthogonal strips on the opposite face of the detector, a uniform position resolution of $5\mu m$ was assumed for z also. The expected degradation of the z resolution with polar angle θ has not been included. It should be emphasised that the xy hits and the z hits from a track were assumed to be completely uncorrelated, i.e. the z information from the silicon was treated completely independently from the xy information. In practice, Landau correlations should provide some degree of association between the xy and z coordinates in a wafer.

The scheme outlined in ref [2] envisages four wafers (chips) along the full length of the detector,

2

with the two chips with $z < 0$ and the two chips with $z > 0$ daisy chained together. Thus, the *sign* of the z coordinate would be known for each xy hit. Similarly, it is assumed in ref [2] that each barrel contains 18 chips making up the full 2π in azimuth. In the two-sided readout case, separate z readout for each chip is assumed. Thus, the *azimuthal* position of each z hit is known to lie within a given window of size $\Delta\phi = 20°$ ($=360°/18$).

The standard ROPE track finding, track matching and track fitting code was used to obtain the charged tracks reconstructed in the existing OPAL detector (program versions ROPE307, CV318, CJ712, CZ311 and CT215). These tracks were then used as input to the silicon analysis. For technical reasons, and in order easily to be able to study the effects of varying the assumed central detector resolutions, for the final track fitting, the spatial positions of the CV,CJ,CZ hits associated to CT tracks were regenerated by smearing about the true track position using Gaussians of fixed width (resolution). The central detector resolutions assumed for this smearing are summarised in table 2. They are intended to be reasonable estimates of the resolutions that will be achieved in OPAL after 1-2 years of running.

Table 2: Hit resolutions assumed for CV,CJ,CZ detectors.

	xy	z
CV axial	60 μm	4.5 cm
CV stereo	2500 μm	860 μm
CJ	130 μm	4.5 cm
CZ	1.5 cm	330 μm

3 Single Track Reconstruction

Single track resolution studies were carried out using single muons generated with GOPAL120 at a fixed polar angle θ of 90° and randomly over the full 2π in azimuth ϕ. The starting point for each muon was fixed at $(x, y, z) = (0, 0, 0)$. Track finding and track fitting was carried out with the standard CV,CJ,CZ,CT code. Results will be given in terms of the standard OPAL track parameters d_0, ϕ_0, p_T, z_0, and $\tan\lambda$ where the impact parameter d_0 is the (signed) distance from $(0,0,0)$ to the point of closest approach (p.c.a.), ϕ_0 is the track direction in the transverse plane at the p.c.a., z_0 is the z position of the track at the p.c.a., and λ is the dip angle of the track [4]. The "transverse" track parameters d_0, ϕ_0, and p_T were determined using the Billoir track fit method [5]. The standard Billoir fit routine [1] was modified to take into account the presence of the extra material introduced by the silicon detector. The "longitudinal" track parameters z_0 and $\tan\lambda$ were found from a standard linear fit of the z positions of the track hits as a function of the arc length s in the xy plane.

The resolution on each of the track parameters (d_0, ϕ_0 etc.) was found by first fitting a Gaussian to the full distribution of that parameter, and then refitting a Gaussian over the range $\pm 3\sigma$ as given by the first fit. Loose quality cuts were placed on the CT tracks used; the reconstructed CT track was required to contain at least 80 CJ hits. In addition, for fits involving CV, the track was required to have at least 6 CV axial hits and 3 CV stereo hits. For fits involving CZ, 3 CZ hits were required. The CJ requirement removed less than 1% of all tracks. The CV and CZ requirements removed typically

---
[1]routine OUBILF in the OU202 PAM file

3

5% and 10% of CT tracks respectively. In fact, the fitting procedure and the quality cuts used are of little significance and simply provide some protection against the occasional badly reconstructed track appearing in the tails of the impact parameter distributions for example.

3.1   Transverse track parameters; d_0, ϕ_0, p_T

Figure 2 shows the impact parameter (d_0) resolution in OPAL for single muons (with reconstructed hits in both CV and CJ) as a function of the muon momentum. The d_0 resolution is shown separately for the existing OPAL detector (dashed curve) and with the addition of the "standard" silicon detector with two barrels at radii of 6cm and 8cm outside a beam pipe of radius 5cm (solid curve). The silicon detector is seen to provide a factor of two improvement in impact parameter resolution at a momentum of 1 GeV, increasing to a factor of $\sim$3 at 15 GeV. At high momentum, the asymptotic values of the impact parameter resolution are $\sim$25μm without silicon and $\sim$5μm with silicon. However, no allowance has been made here for possible uncertainties in the alignment of the silicon detector with the rest of OPAL and, in practice, this will presumably limit the precision which can be achieved at high momentum.

A similar plot of the ϕ_0 resolution as a function of momentum is shown in Figure 3. A small improvement in the ϕ_0 resolution is seen with silicon at low momentum (below $\sim$5 GeV), but the resolutions with and without silicon approach the same value ($\sim$0.1 mrad) at high momentum.

More detailed results, including impact parameter and ϕ_0 resolutions for other combinations of subdetectors (CJ only, SI+CJ etc.) are given in Appendix A (Tables 12 and 13). For tracks found only in the jet chamber (i.e. with no matching CV track) the improvement in d_0 or ϕ_0 resolution with silicon is much larger than that seen in figures 2 and 3. This applies to $\sim$25% of tracks in a multihadron event for example, owing largely to the finite two particle resolution in CV ($\sim$2.5mm).

The momentum resolution $\delta(p_T)/p_T$ obtained with and without silicon is given in table 14 in Appendix A. For CV+CJ tracks, a small improvement in the momentum determination (reaching $\sim$20% improvement at 50 GeV) is obtained at high momentum with the addition of silicon. For tracks with no CV hits, the improvement at high momentum is somewhat larger, almost a factor of 2 at 50 GeV.

3.2 z_0 and θ resolution

Because the z coordinate for charged tracks is relatively poorly measured in OPAL, the improvement in the z_0 resolution obtained with a silicon detector is much greater than that for the transverse impact parameter d_0. Figure 4 shows the z_0 resolution as a function of momentum for full length (CV+CJ+CZ) tracks, with and without silicon. For standard OPAL, the z_0 resolution is $\sim$650μm at a momentum of 1 GeV, falling slowly to an asymptotic value around 400μm at high momentum. With the addition of silicon, (i.e for SI+CV+CJ+CZ) we find a z_0 resolution comparable to the d_0 resolution shown earlier in figure 2, i.e. $\sim$85μm at 1 GeV falling to below 10μm at high momentum. This represents a factor $\sim$7 improvement at 1 GeV, increasing to a factor $\sim$40 at high momentum. However, this improvement in resolution will only be achieved in practice if the z hits in the silicon detector can successfully be matched to the relatively poorly measured charged track reconstructed using the central detector z information. This will be discussed in detail in the next section.

Figure 5 shows the θ resolution, with and without silicon, for single muons for full length (CV+CJ+

+CZ) tracks. The improvement obtained with silicon reaches a factor ~ 2 at low and high momenta. The track direction in the rz view is in fact rather well determined with the present OPAL detector *provided* the reconstructed track contains both CZ hits and CV stereo hits. For less well measured tracks (*e.g.* no CV stereo hits or no CZ hits) the improvement in the z_0 and the θ resolution can be dramatic (see tables 15 to 18 in Appendix A).

3.3 θ dependence

The dependence of the d_0 and z_0 resolutions on the polar angle θ was also studied. For both d_0 and z_0, the resolution was found to increase only slowly with θ, becoming a factor ~ 2 worse at $\theta = 45°$ both with and without silicon. (The silicon resolution in z was assumed to be 5μm for all polar angles θ). Detailed results can be found in Tables 19 and 20 in Appendix A.

3.4 Dependence on geometry and resolution

Finally we consider the dependence of the impact parameter resolution on the silicon detector geometry and on the silicon resolution assumed. In particular, we consider the dependence on the radii and thicknesses of the beampipe and of the silicon barrels, and compare the standard two barrel silicon detector with a one or a three barrel detector. Also studied is the effect on the track resolution of adding a second (outer) beam pipe between the outer silicon barrel and the inside of the central detector.

Detailed results are given in Appendix A (Tables 21 to 28), but we can summarise the results as follows:

1. In general, the impact parameter resolution depends only weakly on the silicon resolution assumed. Doubling the silicon resolution from 5μm to 10μm for example increases the d_0 resolution by 10-20%, but can increase the z_0 resolution by up to $\sim 30\%$.

2. Changing the silicon barrel radii can give significant changes in resolution, but the overall improvement compared to the existing OPAL detector remains around a factor ~ 2. At 1 GeV for example, moving the outer barrel in by 1cm from 8cm to 7cm radius only changes the d_0 resolution from 85μm to 87μm. Moving the inner barrel (and beam pipe) further in by 1cm changes the impact parameter resolution from 85μm to 71μm.

3. The resolution changes only slowly as the thickness of the beam pipe or of the silicon itself is varied. Doubling either the silicon or beam pipe thickness for example gives a $\sim 20\%$ worse impact parameter resolution at 1 GeV.

4. The impact parameter resolution for a single barrel silicon detector (at a radius of 6cm) is slightly better than that for the standard two barrel detector (at radii 6cm and 8cm), the loss of one silicon hit being compensated for by the reduction in multiple scattering with only one barel present. However, a single barrel detector would presumably make the pattern recognition problem more difficult (see below);

5. Adding a third silicon barrel (to give barrel radii of 6,7 and 8cm) gives a slightly poorer impact parameter resolution compared to the standard two barrel detector. Again, the improved precision from the extra silicon hit is outweighed by the extra material of the third barrel, but the main benefit of a third layer would be in the area of pattern recognition.

5

6. Detector geometries based on a 6cm beam pipe have impact parameter resolutions for d_0 which are typically $\sim$20% worse at 1 GeV (and less at higher momenta) than for the "standard" geometry with a 5cm beam pipe. For z_0 the resolution can degrade by more than for d_0 but still represents an enormous improvement compared to the z_0 resolution with the existing OPAL detector. Adding a second beam pipe between the silicon and central detectors has at most a 5% effect on the d_0 or z_0 resolution.

4 Pattern Recognition

We now consider the problem of pattern recognition with a silicon microvertex detector, namely the association (in complex hadronic events) of the observed silicon hits with the charged tracks reconstructed in the OPAL central detector (CV,CJ,CZ).

Most of the studies described in this section were carried out using a sample of 236 B$\bar{\text{B}}$ events generated with LUND 6.3, with the requirement that there be at least two B mesons within $\pm 45°$ $\theta=90°$. (This represents 48% of all $e^+e^- \rightarrow$ b$\bar{\text{b}}$ events generated.) The events were processed with GOPAL120 (with full simulation) and ROPE307.

A display of the silicon plus vertex chamber (CV) region for a B$\bar{\text{B}}$ Monte Carlo event is shown in Figure 6 (where it is seen that the level of noise hits generated in CV in the Monte Carlo is much greater than that experienced at LEP!). This gives some feeling for the pattern recognition task in such events. For the event shown, most tracks can, by eye, clearly be matched with a pair of silicon hits. However there are cases where the association is not so clear cut.

For all results in this section, loose track quality cuts were applied to the reconstructed CT tracks: at least 20 hits on the track, $|d_0| <$5cm, $|z_0| <$ 20cm and $p_T >$ 150MeV. An average of 20.1 CT tracks per event remained after these cuts, 21% of which had no CV hits associated, while 32% had no CZ hits found. Similarly, 43% of all surviving CT tracks had a good quality CV track associated (8 or more CV axial hits and 5 or more CV stereo hits).

4.1 Two-track separation

In these studies, perfect two track resolution for the silicon was assumed. To justify this, Figure 7(a) shows the distribution of the separation Δs between neighbouring silicon hits for the inner (6cm radius) silicon barrel in the B$\bar{\text{B}}$ event sample. Only pairs of hits in the same detector chip were used for this distribution (with 18 chips in azimuth and 2 chips in z). A typical two track resolution for silicon microstrip detectors is about 150μm. From the distribution in figure 7, obtained from the 236 B$\bar{\text{B}}$ events, there were 135 instances where the two hit separation was less than 150μm, i.e. $\sim$0.6 "overlaps" per event, affecting $\sim$4% of tracks in these events.

Similarly, figure 7(b) shows the separation Δz between neighbouring hits for the inner barrel. Again, only pairs of hits in the same detector chip were considered. The number of cases where the two hit separation in z is less than 150μm is $\sim$0.4 per event. Thus, for both the xy and z projections, the number of track overlaps is at a low rate, and, for the present, a finite two-track silicon resolution has not been implemented.

Figure 8(a) shows the distribution of the number of hits per chip for each silicon chip in the inner layer, for the sample of B$\bar{\text{B}}$ events. Just over 70% of the chips in an event are completely empty, while

6

16% contain only one hit, and 12% contain more than one hit. Approximately 80% of all hits are to be found in chips which contain more than one hit.

Figure 8(b) shows the number of hits in the "busiest" (*i.e.* most populated) chip in each $B\bar{B}$ event. The busiest chip typically contains ~ 7 hits.

In addition to genuine hits from charged tracks traversing the silicon, we also expect a number of random noise hits in each event. The effect of noise hits on the pattern recognition will be considered at the end of this section.

4.2 Track extrapolation to silicon

The first step in the pattern recognition is the extrapolation of all CT tracks inwards from the central detector to the inner and outer silicon barrels. Contributions to the track parameter error matrix resulting from material encountered *en route* to the silicon were taken into account as accurately as possible. Care was taken (using single muons along the lines of section 3) to check that the errors computed reflected the actual resolutions on the track position and direction after extrapolation to the silicon.

Figure 9(a) shows the computed error δs in the track position at the outer (8cm radius) silicon barrel for all extrapolated CT tracks in the $B\bar{B}$ event sample, as a function of the track momentum. Two main bands can be seen, the lower band corresponding to tracks containing both CV and CJ hits, the upper band corresponding to tracks where no CV hits were found. The error on the track extrapolation improves with increasing momentum as the amount of multiple scattering decreases. For tracks in the region 1-5 GeV/c with CV hits associated, the extrapolation error at the silicon is $\sim 50\mu m$ or better.

Figure 9(b) shows a similar plot for the error δz on the z position of the track extrapolation at the outer silicon barrel. Again, two clear bands are seen corresponding to tracks with and without CV stereo hits or CZ hits. The precision is clearly somewhat worse for δz than for δs; $\sim 300\mu m$ for full length (CV+CJ+CZ) tracks and $\sim 1000\mu m$ for CV+CJ tracks. The error δz is essentially momentum independent, *i.e.* the multiple scattering contribution is small in comparison with the error due to the central detector resolution itself.

Figure 10(a) shows the computed error on the transverse track *direction* $\delta\phi$ after extrapolation to the silicon detector. This error is given in units of microns per cm of extrapolation. At 2GeV/c for example, the error on the track direction is only $\sim 10\mu m$ per cm, corresponding to a $\sim 20\mu m$ uncertainty over the 2cm lever arm between the inner and outer silicon barrels. A comparison with figure 9(a) shows that the uncertainty in $\Delta s_1 - \Delta s_2$ is smaller than the uncertainty in either Δs_1 or Δs_2 alone. In other words the *alignment* of the silicon hits with the extrapolated track is better determined than the *absolute distance* of either hit from the extrapolated track. This will be of use below in developing pattern recognition algorithms to associate silicon hits to CT tracks.

Figure 10(b) shows a similar plot for the computed error on the track direction in z, in units of microns/cm. The track direction in z is generally known with a precision comparable to that in xy, *e.g.* $10\mu m$ per cm at 2GeV for CV+CJ+CZ tracks, and $\sim 40\mu m$ per cm for CV+CJ tracks. The uncertainty in $\Delta z_1 - \Delta z_2$ is much smaller than the uncertainty in either Δz_1 or Δz_2 alone.

4.3 The nearest hit

The simplest of all possible pattern recognition algorithms is, for each barrel, just to associate the nearest silicon hit to the extrapolated track position at that barrel. This "algorithm" can be applied separately to the xy hits and the z hits, but unfortunately produces a fairly high error rate. For the xy hits in B$\bar{\text{B}}$ events for example, we find that, for tracks which did in fact traverse both silicon barrels and produce two silicon hits, at least one of the silicon hits selected would be the wrong hit for 8% of the tracks (1.5 errors per event). For 72% of these errors, *both* of the silicon hits selected would be the wrong hits. For the z hits, the situation is somewhat worse, the nearest hit being the wrong hit for $\sim$25% of charged tracks (4.5 errors per event).

In addition, errors can also be made whereby hits are assigned to CT tracks which did not in fact leave any silicon hits (e.g. tracks from interactions in material between SI and CV, conversions etc.). This adds about 1 error per event for xy and for z.

There can be some ambiguity in deciding which is the "true" silicon hit corresponding to a given reconstructed CT track, and this will contribute at some level to the pattern recognition error rate. Here, the "true" track associated with a given CT track was taken to be the true track contributing the largest number of CJ hits to the CT track. However, a CT track may contain a significant number of hits from two or more true tracks, or a given true track may give rise to two or more CT tracks.

To try to improve on the error rates found simply by using the nearest hit, a more general (flexible) pattern recognition algorithm was developed which took into account the uncertainty on the track position and direction after extrapolation of the CT track in to the silicon detector. Further, in complex cases, the algorithm could opt not to assign any silicon hits to a track rather than risk making an error. Some results obtained using this more general algorithm are described in the rest of this section.

Any pattern recognition algorithm will inevitably involve a compromise between a low error rate and high efficiency. It is difficult to quantify the maximum error rate that can be tolerated from the pattern recognition as this will ultimately be determined by the requirement that the resulting physics is not degraded significantly.

4.4 Pattern recognition algorithm (xy)

Figure 11 shows a scatter plot of Δs_1 versus Δs_2 for all extrapolated tracks in the B$\bar{\text{B}}$ event sample, where Δs_i is the distance between the extrapolated track position and the true hit position for the i'th barrel (i=1,2). Here, Δs is the distance measured around the barrel (arc length) in the xy plane. A strong correlation is seen between Δs_1 and Δs_2, reflecting the fact noted above that the track direction is in general better determined than the overall track position. In other words, the track is "shifted sideways" from its true position but not "rotated".

This result was used as the basis of an iterative pattern recognition algorithm which looked for pairs of hits lying close to, and aligned with, the extrapolated CT track, i.e. pairs of hits close to the diagonal of figure 11. In early iterations, hits were assigned only to well measured tracks with well known extrapolations and to "clean", relatively unambiguous cases with no confusing nearby tracks or hits. Subsequent iterations then tackled the more poorly measured tracks and the more confusing situations. Details of the implementation of this algorithm are given in Appendix B.

The efficiency and error rate found using this pattern recognition algorithm for the xy hits in the

$B\bar{B}$ event sample are given in the first column (labelled 'xy') of table 3. The error rate is broken down into two components:

1. *Type A errors*, where the *wrong* hit (or hits) is assigned to a track, and the track did in fact produce genuine silicon hits;

2. *Type B errors*, where one or more hits are assigned to a track which in fact had no "true" silicon hits.

Table 3: Efficiencies (in percent) and error rates (number of tracks with errors per event) from the pattern recognition algorithm for the association of xy and z silicon hits. "Type A" and "Type B" errors are defined in the text.

	xy	z	xy and z	xy or z
Efficiency	93%	85%	81%	96%
Error Rate, Type A	0.08	0.25	0.02	0.31
Error Rate, Type B	0.05	0.09	0.02	0.12

The error rate in table 3 is indeed an improvement on that found with the simple "nearest hit" algorithm. In addition, there were no errors at all for 88% of the events, and no inefficiencies (i.e. all tracks with both silicon hits correctly assigned) for 42% of all events.

The efficiencies and error rates given here can undoubtedly be improved with further tuning of the algorithm. Other approaches to pattern recognition could also be tried, for example assigning hits to tracks in a global fashion (*i.e.* for several tracks at once) based on an overall best fit of the extrapolated tracks to the silicon hits.

4.5 Pattern recognition algorithm (z)

Associating the correct silicon hits in the z coordinate to the CT tracks is more difficult than for the xy case because of the poorer measurement of the z coordinate in the OPAL central detector. By comparing figures 2 and 4, we see that even for tracks with associated CV stereo *and* CZ hits, the z_0 resolution is typically a factor $\sim$3-10 worse than the d_0 resolution. However, the uncertainty on the track *direction* is only a factor $\sim$2 worse in the z view than in the xy view. We might therefore hope that a similar pattern recognition algorithm to that described above for the xy case might also work for the z hits.

Figure 12 shows a scatter plot of Δz_1 versus Δz_2 for tracks in $B\bar{B}$ events after extrapolation to the inner and outer silicon barrels, where Δz_i is the difference in z between the true hit and the extrapolated track position for the i'th barrel. The clear correlation seen in the xy case (figure 11) is still seen for z. The pattern recognition algorithm used above for the xy hits can therefore also be used for the z information.

In the z case, the pattern recognition is helped by the fact that each barrel is composed of many (18) separate detectors (chips), each of which has a separate z readout. In other words, the *azimuthal*

position of each z hit is known to within an angular range of $\Delta\phi=360°/18=20°$. This is in contrast to the xy case where only the *sign* of the z coordinate associated with each xy hit is known. This ϕ segmentation of the z readout significantly reduces the number of candidate track/silicon matches in z.

The pattern recognition efficiencies and error rates for z are shown in the second column of table 3. We see that the overall efficiency is reasonably high (85%), and that the error rate is still low.

The last two columns of table 3 show the overlap between the hits found in xy and those found in z. For approximately half of the tracks where the silicon hits were missed in xy, both hits were found successfully in z. Similarly, for approximately half of the tracks with an error in xy, the hits were found successfully in z. Thus, inefficiencies and errors in xy and in z are somewhat uncorrelated.

4.6 Dependence on silicon detector geometry

The pattern recognition algorithm used above is based on the alignment of pairs of silicon hits with the extrapolated tracks, as well as on the distance of the hit from the track. For other geometries than the standard 6cm/8cm geometry, especially those where the two silicon barrels are closer together, or for detectors with a single layer of silicon only, we would expect the pattern recognition performance to be poorer. Efficiencies and error rates for three different detector geometries are summarised in Table 4. The performance with two barrels at 6.5cm and 7.5cm is only slightly worse than for the standard geometry using 6cm and 8cm. Further, the xy pattern recognition works well even with only a single barrel detector, though, in the absence of Landau correlations, the matching to the silicon z information is becoming somewhat marginal.

Table 4: Efficiencies (in percent) and error rates (number of tracks with errors per event) from the pattern recognition algorithm for the association of xy and z silicon hits, for several different silicon detector geometries.

Radius (cm)			Efficiency (%)		Error Rate (per event)	
BP	SI1	SI2	xy	z	xy	z
5.0	6.0	8.0	93%	85%	0.13	0.34
6.0	6.5	7.5	92%	84%	0.24	0.40
6.0	6.5	—	87%	72%	0.80	1.90

4.7 Dependence on central detector resolution

The size of the errors on the track extrapolations to the silicon depend on the hit position resolutions assumed for CV,CJ and CZ. Over optimistic assumptions for these could lead in turn to over optimistic conclusions about pattern recognition performance, especially in z. The pattern recognition was therefore studied with different assumptions for the CZ stereo and CJ z resolutions, with the results

shown in Table 5 (for the double beam pipe geometry with barrel radii of 6.5 and 7.5cm). Doubling the CZ stereo resolution for example gives only slightly poorer efficiencies and error rates in z.

Table 5: Efficiencies and error rates from the pattern recognition algorithm for the association of xy and z silicon hits, for different choices for the z resolution for CV stereo and CJ hits.

z resolution		Efficiency		Error Rate	
CV	CJ	xy	z	xy	z
860μm	4.5cm	92%	84%	0.24	0.40
1500μm	6.0cm	92%	75%	0.26	0.46

4.8 Addition of noise hits

Finally, the effect on the pattern recognition of adding a given number of additional, randomly positioned, silicon noise hits to the event was studied. The extra noise hits were generated uniformly in ϕ and uniformly in z. The results, for a double beam pipe geometry with silicon barrel radii of 6.5cm and 7.5cm, are given in Table 6. The main effect with noise hits present (with the current tuning of the pattern recognition algorithm) is an increase in the error rate for the xy matching, but the efficiencies and error rates are still acceptable even with 200 added noise hits per barrel.

Table 6: Efficiencies and error rates from the pattern recognition algorithm with the addition of random noise hits in the silicon detector.

Radius			Noise Hits	Efficiency		Error Rate	
BP	SI1	SI2		xy	z	xy	z
6.0	6.5	7.5	0	92%	84%	0.24	0.40
			100	91%	82%	0.64	0.40
			200	89%	82%	1.04	0.58

4.9 Summary

In summary, it seems possible to assign the xy silicon hits to the correct CT track with an efficiency of over 90% and with very low error rate without much difficulty. In z also, hits can be matched successfully with only slightly poorer efficiencies and error rates than for xy. This is still true even for detectors with barrels as close together as 1cm, and also in the presence of large numbers of noise hits. For single barrel detectors, the xy silicon hits can still be matched successfully but the z information is probably of only marginal use.

5 Vertex Reconstruction

In this section we compare the resolution which can be obtained on the position of primary and secondary (decay) vertices with the existing OPAL detector and with a silicon detector added. No attempt will be made at vertex *finding*; instead we will "cheat" and determine which of the CT tracks in a given event did in fact come from the primary vertex, or from a B or D decay.

The (x, y) position of each vertex was determined using the same fitting procedure [6] as employed in the standard CX ROPE processor, namely by minimising the quantity $\chi^2 = \sum D_i^2/\sigma_i^2$ where D_i is the perpendicular distance (in the xy plane) from track i to the vertex position, and σ_i is the error on D_i. The z vertex coordinate is then computed as the weighted average of the z positions of all the tracks at the fitted (x, y) position: $z = (\sum z_i/\sigma_i^2)/(\sum 1/\sigma_i^2)$ where now σ_i is the error on z_i.

The average p_T for the B's in these events is 32 GeV, while the average p_T for D's is 14.6 GeV. The average true flight path for B's is 2.2mm and for D's is 1.3mm.

Figure 13 is an event display of the vertex region of the B$\bar{\text{B}}$ event shown earlier in figure 6, with the secondary vertices clearly visible.

All results in this section are for the sample of 236 B$\bar{\text{B}}$ events with at least two B mesons within $\theta = \pm 45°$. Standard track quality cuts were applied to the CT tracks, and the pattern recognition algorithm described in the previous section was used to associate silicon hits to charged tracks.

5.1 Primary vertex resolution

Figure 14 shows the distributions of reconstructed x and z coordinates for the primary vertex in B$\bar{\text{B}}$ events, both for the existing OPAL detector and with the addition of a silicon microvertex detector. Only those tracks known from the GOPAL "cheat word" information to come from the primary vertex were used. We see a clear improvement in position resolution for both the x and z vertex coordinates once silicon is included. Further, with the silicon microvertex detector added, the position resolution for z is now comparable to that for x. Estimates of the primary vertex position resolution derived from these distributions are summarised in table 7.

Table 7: Resolutions (in μm) on primary vertex position for u$\bar{\text{u}}$ and B$\bar{\text{B}}$ events, with and without silicon.

	avg. mult	No Silicon		With Silicon	
		xy	z	xy	z
b$\bar{\text{b}}$	8.8	130	550	80	80
u$\bar{\text{u}}$	17.3	70	300	30	30

Also given in Table 7 are the primary vertex resolutions found for a sample of LUND u$\bar{\text{u}}$ events. The average multiplicity of primary vertex tracks (=17.3) is much higher for these events than for the B$\bar{\text{B}}$ sample (=8.8), and the primary vertex position resolution is significantly better. The improvement in resolution with silicon is similar to that found for B$\bar{\text{B}}$ events.

12

5.2 B and D decay vertex resolution

Figure 15(a) shows distributions of the difference between the true and reconstructed B decay vertex position, projected onto axes along and perpendicular to the true direction of the B flight path. The plots are shown for the xy projection only, with and without the silicon microvertex detector. Only those tracks which genuinely came *directly* from the decay of the B meson itself were used in the vertex fit (any D meson daughters were excluded). The plot is for inclusive B decays to two or more charged particles. As would be expected from the collimation of the B decay products due to the high B transverse momentum (32 GeV on average), the position resolution transverse to the B direction is much better than that along the B flight path. Significant improvements in resolution are seen with silicon added, similar to those seen above for the primary vertex.

A similar analysis was carried out for D decay vertices in the $B\bar{B}$ sample. Estimates of the B and D decay vertex position resolutions, with and without silicon, are summarised in Table 8. The average charged multiplicity for the B vertices was 3.5, compared to 2.6 for D vertices.

Table 8: Resolutions (μm) on B and D vertex position, projected along and perpendicular to B or D flight path, with and without silicon.

	avg. mult	No Silicon			With Silicon		
		xy (along)	xy (perp)	z	xy (along)	xy (perp)	z
B	3.5	750	100	470	350	40	120
D	2.6	860	70	530	500	40	110

5.3 B and D Flight Paths

Figure 16 shows scatter plots of the true versus the reconstructed flight path for B mesons, with and without silicon, where the "flight path" is the distance between primary vertex and B decay vertex in xy plane only. Figure 17 shows similar plots for the full 3D flight path. In both cases, a clear improvement is seen in the resolution on the flight path measurement.

Figure 18 shows the distributions of the quantity Δ=true minus reconstructed flight path, both for the xy projection only, and for the full 3D flight path. The dashed histograms are with the existing OPAL detector, the solid histograms are with the addition of silicon.

A measure of the significance of the flight path measurement is given by the quantity K defined as the ratio K=true flight path / rms error on flight path. Figure 19 shows the K distribution for all B flight paths, for the xy projection only ("2D") and with z included ("3D"), with and without silicon. A clear shift towards larger values of K is seen with the silicon detector present. There are no significant differences between the 2D and 3D distributions.

Table 9 gives a breakdown of these K distributions into the fractions of $B\bar{B}$ events with $K < 2$, $2 < K < 5$ and $K > 5$. The larger the value of K, the better are the prospects for vertex finding.

Loosely speaking, for intermediate values of K we might hope to tag the event as containing a B or D decay, while for large values of K there would be some chance of partially or fully reconstructing the decay vertex. From Table 9 we see a factor ~ 3 increase in the fraction of B's in the "vertex finding" ($K>5$) category with silicon.

Table 9: Fraction of B$\bar{\text{B}}$ events with $K < 2$, $2 < K < 5$, $K > 5$ with and without silicon, where K=true flight path / rms error on flight path.

		No SI (%)	With SI (%)
$K > 5$	"Vertex Finding"	10	31
$2 < K < 5$	"Tagging"	22	31
$K < 2$	"??"	67	38

Finally, the position resolution for primary and secondary vertices was studied using the *true* silicon hit(s) for each track instead of using the hits found by the pattern recognition algorithm. No significant differences in resolution were observed. We note also that using the pattern recognition algorithm sometimes gave a more accurate vertex reconstruction than when the true hits were used, for example when tracks are badly reconstructed in CV and/or CJ it is often better *not* to add the silicon hits to the track since the overall SI+CV+CJ fit is then distorted.

6 Towards B-tagging Using Track Impact Parameters

In this section, we consider the improvement a silicon detector might provide for tagging B events via the presence of tracks with large reconstructed impact parameter. A full B-tagging analysis would have to consider various problems due to "fake" large impact parameters from badly reconstructed tracks, tracks from interactions and conversions *etc.*. Here we simplify the problem by only considering tracks known (using the GOPAL "cheat" information) to have come from the primary vertex or from the decay of a B or D hadron.

We first consider the impact parameter as measured with respect to the *true* primary vertex position (i.e. $x=y=z=0$). This avoids potential problems from bad vertex reconstruction, and relies only on the correct reconstruction and error determination for individual charged tracks. Below, we consider also the impact parameter measured with respect to the *reconstructed* primary vertex.

To indicate the precision required on d_0 and z_0 for B and D tagging, figure 20 shows the distribution of *true* impact parameters (to the true primary vertex) for charged tracks from B and D decays. Almost half the tracks from B decays have impact parameters below 100μm, with 24% having d_0 greater than 300μm. The distribution for D decay secondaries is somewhat broader; 34% have d_0 below 100μm while 34% have d_0 above 300μm.

We define the significance N_σ of the measurement of the impact parameter d_0 as $N_\sigma = d_0/\sigma(d_0)$. Similarly, for z_0 we define $N_\sigma = z_0/\sigma(z_0)$.

As a check that the errors $\sigma(d_0)$ and $\sigma(z_0)$ are computed reliably, figure 21 shows the distributions

of N_σ for primary vertex tracks, with and without silicon. These distributions can all be reasonably represented by Gaussians of width unity (indicating that the errors on the measured impact paramater have been computed correctly), though there are tails from poorly reconstructed tracks. We also see that for z, the N_σ distribution without silicon (i.e. for existing OPAL) is too broad, reflecting the fact that the z errors are underestimated in this case. However, this can only lead in turn to an *underestimate* of the improvement due to the silicon detector.

The N_σ distributions for tracks from B and D decays, with and without silicon, are shown in figure 22. The improvement from silicon can be clearly seen - the fraction of tracks from B (D) decays with a measured impact parameter d_0 more than 5 standard deviations from the true primary vertex position increases from 12% (17%) to 28% (37%) for example with the addition of silicon. For z_0 the improvement is greater because of the relatively poor z measurement in existing OPAL; without silicon, 4% (4%) of tracks are more than 5 sigma from the primary vertex for B (D) decays, but these fractions become 22% (32%) with silicon.

To quantify further the improvement in "B-tagging", we consider the number N of reconstructed charged tracks in an event with $N_\sigma > 3$, i.e. the number of tracks more than 3 standard deviations from the true primary vertex. The first row of Table 10 for example shows the fraction of $B\bar{B}$ events with $N \geq 3$, (i.e. containing at least three tracks with $N_\sigma > 3$), with and without silicon. These fractions are given for the xy and z projections separately, and also for the combinations xy and/or z.

Table 10: Fraction (in percent) of $B\bar{B}$ events containing more than a given number of tracks more than three standard deviations ($N_\sigma > 3$) from the true primary vertex position. The first two rows are for all tracks in the event. The third and fourth rows are for B and D decays with charged multiplicity ≥ 3.

	No SI				With SI			
	xy	z	xy and z	xy or z	xy	z	xy and z	xy or z
$N \geq 3$	57	28	2	79	81	74	53	91
$N \geq 6$	8	2	0	28	34	27	11	57
B, $N \geq 3$	6	0	0	10	27	18	9	41
D, $N \geq 3$	10	2	0	13	37	33	17	60

Subsequent rows in table 10 give, for B and D decays with at least three detected charged tracks, the fraction of these decays where at least three tracks have $N_\sigma > 3$. We see that the fraction of events with several large impact parameter tracks, and the fraction of B or D decays where three or more tracks have large impact parameters, can increase substantially with a silicon detector. The improvement is particularly marked when z information is also available.

The numbers given above were determined using the true primary vertex position, $(x, y, z) = (0, 0, 0)$. We now repeat the analysis leading to Table 10 but using the reconstructed primary vertex position instead (though still using only *known* primary vertex tracks in the vertex fit). We define N_σ

as before, but now also include the contribution from the vertex error itself in the error calculation:

$$N_\sigma = \frac{d_0}{\sqrt{\sigma_{track}^2 + \sigma_{vert}^2}}$$

The results are given in table 11. Though the improvements due to silicon are now reduced, as would be expected from the smearing of the primary vertex position used, the overall conclusions remain unchanged.

Table 11: Same as table 10 but using the measured primary vertex position instead of the true position.

	No SI				With SI			
	xy	z	xy and z	xy or z	xy	z	xy and z	xy or z
$N \geq 3$	36	24	4	57	63	64	30	81
$N \geq 6$	9	5	1	20	16	21	5	38
B, $N \geq 3$	9	0	0	12	19	17	6	35
D, $N \geq 3$	10	2	1	13	21	28	9	48

Clearly, a much more detailed analysis would be needed to quantify fully the improvement in B-tagging efficiency and in sample purity that could be achieved by adding a silicon vertex detector to OPAL. Neverthelss, the results above seem to indicate that the potential gain from a silicon detector could be quite large, especially if two-sided readout can be used.

7 Summary and Conclusions

In this note, we have studied the potential impact of a silicon microvertex detector on track and vertex reconstruction in OPAL, and tried to indicate the improvement such a detector might have for $B\bar{B}$ physics.

This was done largely assuming a "standard" silicon detector consisting of two silicon barrels at radii 6cm and 8cm sitting outside a reduced beam pipe of radius 5cm. The possibility that the detector might provide high precision ($\sim 5\mu m$) hits in the z direction ("two-sided readout") as well as in the xy projection only ("single-sided readout") was considered in some detail.

For the main "figure of merit" of such a detector, namely the impact parameter resolution, a factor of 2 or more improvement was found in xy at all momenta, and a factor 2-10 was found in z. This improved resolution was reflected also in improved position resolutions for primary and secondary (B or D decay) vertices, and in improved measurement of B and D flight paths.

Perhaps the most important results however concerned the question of pattern recognition with a silicon detector, i.e. whether the silicon hits could be associated correctly to the charged tracks reconstructed in the central detector, especially in z where the resolution for charged tracks is relatively poor. The conclusions, based on studies of $B\bar{B}$ events simulated using GOPAL, are that silicon hits can be matched to charged tracks with good efficiency and low error rate, both in xy *and* in z. Thus two-sided silicon detectors are indeed a possibility for OPAL.

Impact parameter resolutions for geometries based on a 6cm radius beam pipe are typically 10-20% worse at low momentum than for a 5cm beam pipe, but pattern recognition efficiencies and error rates are essentially unchanged. Resolutions for detectors with only a single silicon barrel are comparable to those with two barrels, and pattern recognition in xy is still possible with good efficiency.

A lot of work remains to be done to quantify in detail the gain for physics, in parallel with using the experience gained in B physics analyses on data currently being taken with the existing OPAL detector. However, a study related to the tagging of $B\bar{B}$ events via high impact parameter tracks suggests that significant gains can be made, especially if two-sided detectors can be used.

References

[1] G. von Holtey, Machine Induced Particle Backgrounds at LEP, LEPC talk, March 1988.

[2] A scheme for upgrading the central tracking of OPAL by the addition of an inner silicon microvertex detector, OPAL Report, Sept 1988.

[3] O.Runolfsson, various notes

[4] CV primer for example

[5] P.Billoir, Nucl. Inst. Meth. **225** (1984) 352

[6] CX primer

Figure Captions

Figure 1: Schematic view of a two barrel silicon microvertex detector.

Figure 2: Impact parameter resolution as a function of momentum for single muons at $\theta=90°$, for the existing OPAL detector and with the addition of a silicon vertex detector.

Figure 3: Resolution on track direction ϕ_0 as a function of momentum for single muons at $\theta=90°$, with and without the addition of a silicon vertex detector. The right-hand axis shows the corresponding uncertainty in s_1-s_2.

Figure 4: z_0 resolution as a function of p_T for single muons at $\theta = 90°$, with and without the addition of a silicon vertex detector.

Figure 5: Resolution in polar angle θ as a function of momentum for single muons at $\theta = 90°$, with and without the addition of a silicon vertex detector. The right-hand axis shows the corresponding uncertainty in z_1-z_2.

Figure 6: Graphical display of a $B\bar{B}$ event showing the hits in the silicon (SI) and vertex (CV) detectors and the reconstructed CT tracks from the CV,CJ,CZ detectors.

Figure 7: Distribution of separations (a) Δs and (b) Δz between neighbouring silicon hits in the inner barrel in a sample of $B\bar{B}$ events.

Figure 8: (a) distribution of the number of hits in each chip of the inner silicon barrel in $B\bar{B}$ events. (b) distribution of the *maximum* number of hits in any one chip of the inner barrel.

Figure 9: Scatter plots of the errors (a) δs and (b) δz on the track position after extrapolation to the outer silicon barrel versus p_T, for extrapolated charged tracks in $B\bar{B}$ events.

Figure 10: Scatter plot of the computed errors on the direction of charged tracks after extrapolation to the silicon versus p_T, (a) for xy and (b) for z.

Figure 11: Scatter plot of $(\Delta s)_1$ versus $(\Delta s)_2$ for all extrapolated CT tracks after extrapolation to the two barrels of the silicon microvertex detector.

Figure 12: Scatter plot of $(\Delta z)_1$ versus $(\Delta z)_2$ for all extrapolated CT tracks after extrapolation to the two barrels of the silicon microvertex detector.

Figure 13: Magnified view of the $B\bar{B}$ event of figure 6 showing the primary and decay vertices in the event.

Figure 14: Distribution of reconstructed x and z coordinates for the primary vertex in $B\bar{B}$ events. The solid (dashed) histograms are the results with (without) a silicon vertex detector.

Figure 15: Distribution of true minus reconstructed position of B and D decay vertices (a) along and (b) perpendicular to the true direction of flight of the B or D meson. The solid (dashed) histograms are the results with (without) a silicon vertex detector.

Figure 16: Scatter plots of true versus reconstructed B and D flight paths in the xy plane, (a) without and (b) with silicon microvertex.

Figure 17: Scatter plots of true versus reconstructed B and D flight paths, 3D, (a) without and (b) with silicon microvertex.

Figure 18: Distribution of Δ=reconstructed minus true flight path for B and D decays, (a) without and (b) with a silicon microvertex detector.

Figure 19: Distribution of K=true flight path / error for B and D decays, for 2D and 3D, with and without a silicon microvertex detector.

Figure 20: Distributions of true impact parameter d_0 for tracks from D decays (dashed histogram) and B decays (solid histogram) in $B\bar{B}$ events.

Figure 21: N_σ for primary vertex tracks, (a) xy and (b) z, with and without silicon.

Figure 22: N_σ for tracks from B and D decays, (a) xy and (b) z, with and without silicon.

8 Appendix A

8.1 d_0, ϕ_0 and p_T resolutions

Impact parameter resolutions obtained from single muons for tracks in CJ only and for CV+CJ are summarised in Table 12. (The statistical errors here and for all subsequent tables are typically 5%.) Similar results for the resolutions on the track direction ϕ_0 and on the (inverse) track momentum $1/p_T$ are given in tables 13 and 14.

Table 12: Impact parameter (d_0) resolutions for single muons for CJ and CV+CJ detectors, with and without addition of silicon hits.

p_T (GeV)	CJ only (μm)	CV+CJ (μm)	SI+CJ (μm)	SI+CV+CJ (μm)
1	494.0	178.9	85.6	84.7
2	278.7	102.1	49.3	47.8
5	143.7	51.3	24.9	23.5
10	97.3	34.2	14.9	14.3
15	82.2	30.4	11.2	11.0
50	64.9	25.8	6.1	6.1

Table 13: Resolutions on the track direction ϕ_0 obtained for single muons for CJ and CV+CJ detectors, with and without addition of silicon hits.

p_T (GeV)	CJ only (mrad)	CV+CJ (mrad)	SI+CJ (mrad)	SI+CV+CJ (mrad)
1	2.66	1.78	1.53	1.49
2	1.55	1.21	0.85	0.82
5	0.60	0.41	0.40	0.39
10	0.39	0.28	0.23	0.22
15	0.26	0.17	0.16	0.16
50	0.19	0.10	0.07	0.07

Table 14: Resolutions on $1/p_T$ obtained for single muons for CJ and CV+CJ detectors, with and without addition of silicon hits.

p_T (GeV)	CJ only (%)	CV+CJ (%)	SI+CJ (%)	SI+CV+CJ (%)
1	1.88	1.78	1.80	1.76
2	2.07	1.89	1.89	1.86
5	2.14	1.95	1.91	1.87
10	2.54	2.18	2.13	2.12
15	3.00	2.44	2.22	2.17
50	6.00	3.87	3.24	3.16

8.2 z_0 and θ resolution

z_0 resolutions for all combinations of CV,CJ,CZ subdetectors involving CJ are given in table 15. The resolutions for the same combinations with silicon hits added are given in table 16.

With the silicon microvertex detector present, and for particle momenta below ~ 10 GeV/c, the best z_0 resolution is in fact achieved with the subdetector combinations SI+CJ and SI+CV+CJ, rather than SI+CJ+CZ or SI+CV+CJ+CZ, *i.e.* adding the z-chambers into the track fit actually degrades the resolution. From special runs made with the multiple scattering process in GEANT switched off, This was found to be due to multiple scattering in the material between the CJ and CZ detectors not being taken account of in the sz linear fit.

Table 15: Resolutions on z_0 obtained for single muons for detector combinations involving CJ for the existing OPAL detector (no silicon).

p_T (GeV)	CJ only (μm)	CV+CJ (μm)	CJ+CZ (μm)	CV+CJ+CZ (μm)
1	9420	928	6960	650
2	9140	915	6120	451
5	8640	913	5730	414
10	9220	849	5740	388
15	9770	888	5760	392
50	9420	824	5660	376

Table 16: Resolutions on z_0 obtained for single muons for detector combinations involving CJ, with silicon hits added.

p_T (GeV)	SI+CJ (μm)	SI+CV+CJ (μm)	SI+CJ+CZ (μm)	SI+CV+CJ+CZ (μm)
1	84.9	85.7	217.4	218.2
2	47.5	47.7	95.8	96.7
5	30.0	29.4	41.4	40.4
10	25.3	25.3	20.4	20.4
15	25.4	25.0	13.9	14.0
50	24.1	23.7	7.2	7.3

θ resolutions for all combinations of CV,CJ,CZ subdetectors involving CJ are given in table 17. The resolutions for the same combinations with silicon hits added are given in table 18.

Table 17: Resolutions on θ obtained for single muons for detector combinations involving CJ for the existing OPAL detector (no silicon).

p_T (GeV)	CJ only (mrad)	CV+CJ (mrad)	CJ+CZ (mrad)	CV+CJ+CZ (mrad)
1	8.71	4.46	4.94	2.98
2	7.73	3.66	3.67	1.57
5	7.73	3.40	3.07	0.60
10	7.71	3.38	3.04	0.37
15	7.83	3.34	3.08	0.28
50	7.37	3.33	2.99	0.22

Table 18: Resolutions on θ obtained for single muons for detector combinations involving CJ, with silicon hits added.

p_T (GeV)	SI+CJ (mrad)	SI+CV+CJ (mrad)	SI+CJ+CZ (mrad)	SI+CV+CJ+CZ (mrad)
1	1.51	1.51	3.25	3.25
2	0.81	0.82	1.45	1.45
5	0.46	0.46	0.61	0.61
10	0.37	0.37	0.30	0.30
15	0.37	0.36	0.20	0.20
50	0.34	0.33	0.09	0.09

8.3 θ dependence

Tables 19 and 20 show the dependence of the impact parameter and z_0 resolutions on the polar angle θ, with and without a silicon microvertex detector. The $\theta=40°$ point lies beyond the coverage of the OPAL z-chambers.

Table 19: Variation of d_0 and z_0 resolutions with track polar angle θ, for existing OPAL detector (no silicon) for CV+CJ+CZ tracks.

p_T (GeV)	No Silicon							
	d_0 resolution (μm)				z_0 resolution (μm)			
	$\theta=90°$	$\theta=70°$	$\theta=50°$	$\theta=40°$	$\theta=90°$	$\theta=70°$	$\theta=50°$	$\theta=40°$
1	178.9	229.1	283.0	367.8	650	757	1092	1612
15	30.4	36.9	37.5	44.8	392	411	417	994

Table 20: Variation of d_0 and z_0 resolutions with track polar angle θ, with silicon microvertex detector, for SI+CV+CJ(+CZ) tracks. (CZ was not used for z_0 numbers for p_T below 10 GeV/c).

p_T (GeV)	With Silicon							
	d_0 resolution (μm)				z_0 resolution (μm)			
	$\theta=90°$	$\theta=70°$	$\theta=50°$	$\theta=40°$	$\theta=90°$	$\theta=70°$	$\theta=50°$	$\theta=40°$
1	84.7	97.9	130.3	167.3	85.7	96.7	153.6	232.2
15	11.0	11.2	14.9	17.7	14.0	17.0	26.8	30.2

8.4 Silicon resolution

Table 21 shows the impact parameter resolution as a function of the assumed silicon hit resolution, for single muons at $\theta=90°$. The dependence on the silicon resolution is found to be small. At low p_T, doubling the assumed resolution from 5μm to 10μm for example leaves the d_0 resolution unchanged within the statistical errors (typically 3-4%). At high momentum, the d_0 resolution worsens by $\sim 25\%$.

Table 21: Variation of d_0 and z_0 resolutions with assumed silicon hit resolution, for a beam pipe radius of 5cm and silicon radii of 6cm and 8cm.

p_T (GeV)	d_0 silicon resolution				z_0 silicon resolution			
	5 μm	10 μm	20 μm	50 μm	5 μm	10 μm	20 μm	50 μm
1	84.7	91.2	101.4	131.6	85.7	96.0	114.0	170.4
5	23.5	28.3	34.0	47.2	29.4	41.0	43.9	58.9
15	11.0	13.8	20.0	28.7	14.0	15.5	21.0	42.3

8.5 Detector Geometry

Table 22 shows the variation in impact parameter resolution for full length SI+CV+CJ tracks as the radius of the outer layer of silicon is varied between 6.5cm and 9.0cm, while keeping the inner layer fixed at 6cm radius. No significant variation in resolution is seen; the improvement from silicon comes entirely from having a single high precision hit as close as possible to the interaction point.

To emphasise this, the last column of table 22 shows the d_0 resolution with no outer barrel at all. If anything, the resolution improves slightly, presumably because of the smaller amount of material present for a single barrel detector.

Table 22: Variation of impact parameter resolution with radius of outer silicon barrel. The inner silicon barrel and the beam-pipe were kept fixed at radii of 6cm and 5cm respectively. The last column corresponds to having no outer barrel at all, i.e. a single barrel silicon microvertex detector at a radius of 6cm outside a beam pipe of radius 5cm.

p_T	inner / outer barrel radius			
(GeV)	6.0/6.5 cm	6.0/7.0 cm	6.0/8.0 cm	6.0/— cm
1	92.7	87.2	84.7	81.7
5	24.0	27.4	23.5	20.0
15	9.9	11.2	11.0	11.0

Table 23: Variation of impact parameter resolution with radius of beam-pipe and inner silicon barrel (with a constant difference in radius of 1cm between the beam-pipe and the inner silicon barrel). The outer silicon barrel was kept fixed at radius of 8cm.

p_T	beam-pipe radius / inner barrel radius		
(GeV)	4.0/5.0 cm	5.0/6.0 cm	6.0/7.0 cm
1	70.6	84.7	101.7
5	19.3	23.5	29.0
15	9.3	11.0	12.1

Table 24 shows the impact parameter resolution for several different possible silicon geometries associated with a beam pipe of radius 6cm, rather than the "standard" radius of 5cm. The first three columns of Table 24 correspond to two-barrel geometries with different separations between the inner and outer barrel. The fourth column is for a single silicon barrel at a radius of 6.5cm. The last column is for a two barrel detector with barrel radii 6.5 and 7.5cm, with a second beam pipe at a radius of 8cm (in addition to the inner beam pipe at a radius of 6cm) of thickness 0.1cm of carbon fibre (0.46% radiation lengths). No significant worsening of the impact parameter resolution is seen with this second beam pipe added.

Table 25 gives also the z_0 resolutions for two of these geometries, namely for two barrels at 6.5 and 7.5cm both with and without the second beam pipe at 8cm.

Table 24: Impact parameter resolution for several possible silicon geometries with a beam pipe radius of 6cm. The fourth column corresponds to a single barrel detector of radius 6.5cm. The last column (with barrel radii of 6.5cm and 7.5cm) has an additional (second) beam pipe added at a radius of 8cm.

p_T	d_0 resolution				
	inner / outer barrel radius				
(GeV)	6.5/7.0 cm	6.5/7.5 cm	6.5/8.0 cm	6.5/— cm	6.5/7.5 +BP2
1	116.2	101.7	102.1	101.5	101.7
5	29.2	27.1	28.2	25.8	28.4
15	11.9	11.6	12.2	11.9	12.1

Table 25: Resolutions on z_0 for a two barrel silicon detector with radii 6.5cm and 7.5cm. The second set of numbers includes also a second beam pipe at a radius of 8cm.

		z_0 resolution			
	p_T (GeV)	SI+CJ (μm)	SI+CV+CJ (μm)	SI+CJ+CZ (μm)	SI+CV+CJ+CZ (μm)
single beam pipe	1	102.2	101.8	226.9	231.6
	5	52.1	50.3	42.9	43.2
	15	49.1	47.1	15.4	15.4
double beam pipe	1	105.4	107.3	236.0	238.1
	5	51.1	50.2	45.9	45.9
	15	49.0	48.6	16.1	16.2

Table 26 gives the impact parameter resolution as the radius of the beam-pipe is varied for the *existing* OPAL detector, i.e. taking advantage of a smaller beam-pipe without instrumenting the extra space which then becomes available. We see that, although some improvement in impact parameter resolution can be achieved, this is small in comparison with that obtainable with silicon as well.

Table 26: Variation of impact parameter resolution with beam-pipe radius for the *existing* OPAL detector. The beam-pipe thickness was taken to be 0.1cm of carbon fibre.

p_T	beam-pipe radius			
(GeV)	4.0 cm	5.0 cm	6.0 cm	8.0 cm
1	143.6	148.2	156.8	166.6
5	50.8	51.0	51.6	51.3
15	32.3	32.5	32.6	30.4

Table 27 gives the impact parameter resolution as a function of momentum for a 3-barrel silicon detector with radii 6,7 and 8cm. The d_0 resolution for the standard two-barrel geometry is given again for comparison. We see that the resolution is in fact slightly poorer with the extra barrel added, presumably because the extra precision point doesn't compensate for the additional multiple scattering which is introduced.

Table 27: Variation of impact parameter resolution with momentum for a 3-barrel silicon detector with barrel radii 6,7 and 8 cm.

p_T (GeV/c)	3-barrel (r=6,7,8 cm)	2-barrel (r=6,8 cm)
1	90.6	84.7
5	25.8	23.5
15	10.8	11.0

8.6 Amount of material

Table 28 shows the variation in impact parameter resolution with the assumed thickness of the beam-pipe and of the silicon layers, for a beam pipe radius of 5cm and silicon radii of 6cm and 8cm. The first column in table 28 (zero beam-pipe thickness) corresponds approximately to a silicon detector placed inside the vacuum pipe.

Table 28: Variation of impact parameter resolution with thickness of beam-pipe and silicon layers.

p_T (GeV)	beam-pipe thickness				silicon thickness			
	0.0 cm	0.1 cm	0.15 cm	0.2 cm	250 μm	450 μm	750 μm	1000 μm
1	67.5	84.7	91.9	102.5	73.7	84.7	97.8	110.0
5	21.4	23.5	26.4	27.2	21.6	23.5	26.3	27.7
15	10.2	11.0	11.5	12.2	10.6	11.0	12.2	13.1

9 Appendix B

9.1 Pattern Recognition Algorithm

We give here the details of the pattern recognition algorithm used to associate silicon hits to the charged tracks reconstructed in the OPAL central detector.

The pattern recognition was carried out in several iterations. Each iteration is identical except that the values of certain parameters, namely δ, δ_{veto}, N and N_{veto} could be varied at each step. The algorithm is described below for the association of xy hits, with Δs_1 and Δs_2 being the distances between the extrapolated track position and silicon hits in the inner and outer barrels respectively. The algorithm can also be applied in z using Δz_1 and Δz_2 in place of Δs_1 and Δs_2.

At each iteration:

1. tracks are considered as candidates for hit association only if their extrapolation error at t⁺ outer silicon barrel is less than a fixed amount, δ microns.

2. all pairs of silicon hits are found where both the hits lie within N standard deviations of the extrapolated track, both for the displacements Δs_1, Δs_2 and for the alignment $\Delta s_1 - \Delta s_2$. Track/hit combinations found so far are classed as good match candidates.

3. find all track/hit *veto* combinations as in steps 1 and 2 but requiring the track extrapolation error to be less than δ_{veto} (instead of less than δ) and the hits to be within N_{veto} standard deviations of the track (instead of N).

4. assign the hits to the track for the good match candidates *provided* there are no ambiguities, (*i.e.* provided there is a unique hit which can be matched to the track in each barrel and provided two good tracks do not try to assign the same hits), and provided the match is not vetoed, (*i.e.* provided no veto track/hit combination involves the same hits).

5. in ambiguous cases, *i.e.* more than one possible pair of hits is found for a given track, or a silicon hit is a candidate for association to more than one track, either: don't assign any hits to the tracks involved, or: select the pair of hits with the smallest value of $\Delta s_1 - \Delta s_2$ (i.e. the hit with the best alignment with the track extrapolation).

As well as varying the parameters δ, δ_{veto}, N and N_{veto}, the action to be taken in step 5 could also be varied at each iteration.

For simplicity, each silicon hit could be associated to at most one CT track, and silicon hits were only associated to track in pairs, i.e. no attempt was made to associate hits from a single barrel only.

In xy for example, the first iteration assigned pairs of hits within 2 sigma of any track with extrapolation error less than 100 microns provided there were no ambiguities and neither hit was within 10 sigma of a track with an extrapolation error less than 5000 microns. The last (tenth) iteration assigned the nearest hits to any track with an extrapolation error below 1000 microns provided the hits were within 10 sigma of the track, regardless of any other nearby hits or tracks.
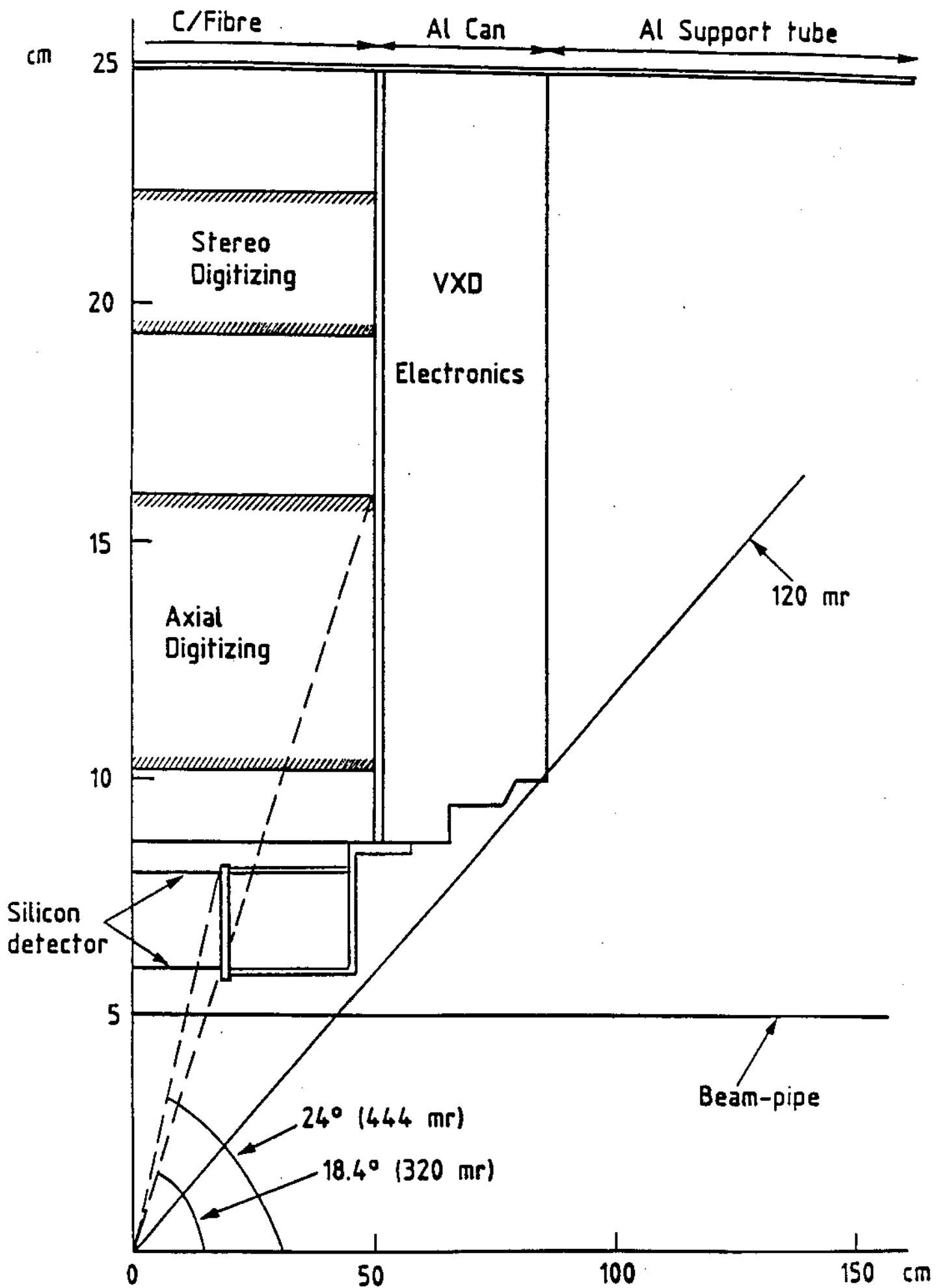
Figure 1   Schematic View of Vertex Region

Figure 2

Impact Parameter Resolution Versus P$_T$

Single Muons, $\theta = 90°$

Figure 3

Track Direction Resolution Versus P_t

Single Muons, $\theta = 90°$

Resolution (mrad)

CV + CJ

SI + CV +CJ

P_t (GeV)

Figure 4

Z_e Resolution Versus P_r

Single Muons, $\vartheta = 90°$

CV + CJ + CZ

SI + CV + CJ (+ CZ)

Figure 5

ϑ Resolution Versus P_T

Single Muons, ϑ = 90°

CV + CJ + CZ

SI + CV + CJ (+ CZ)
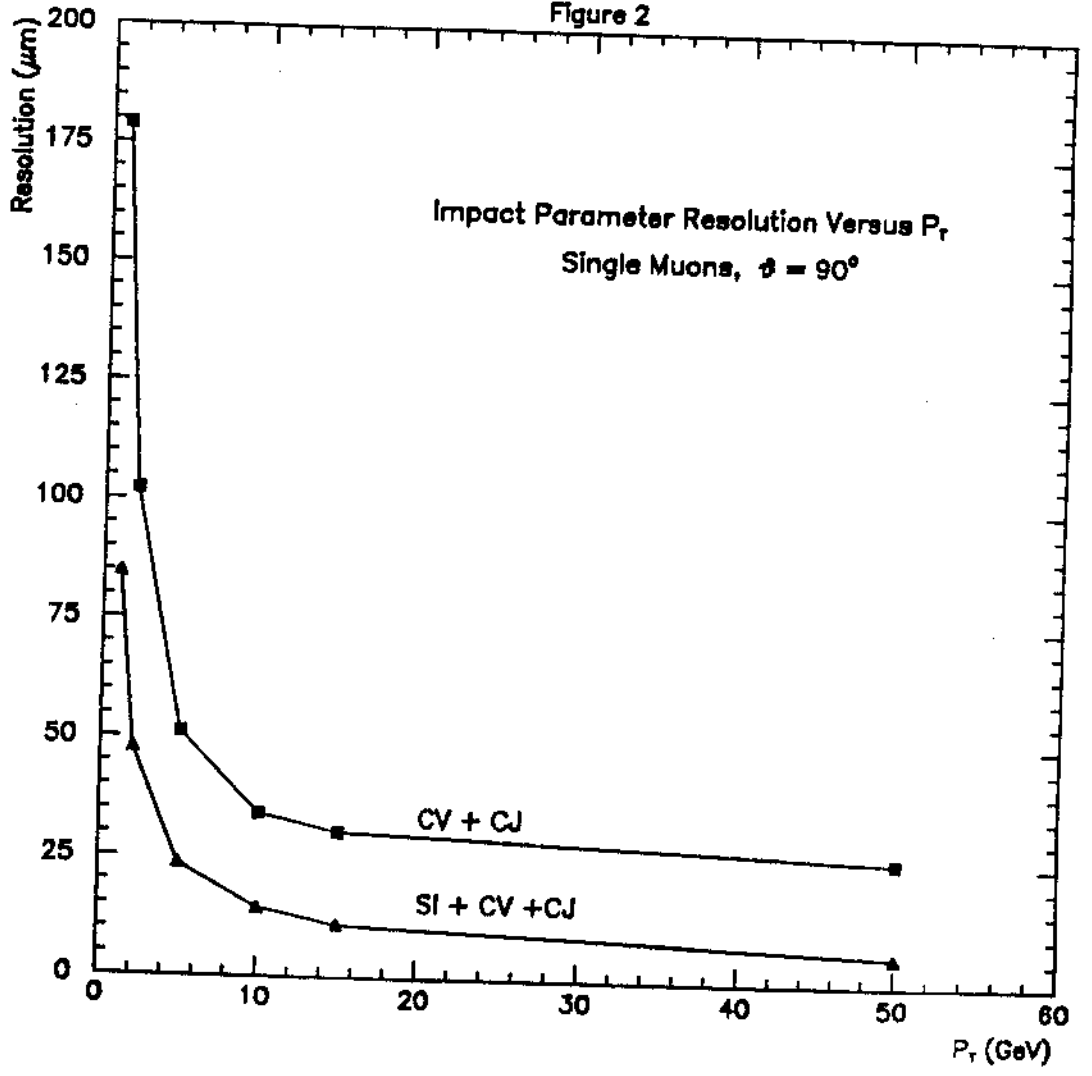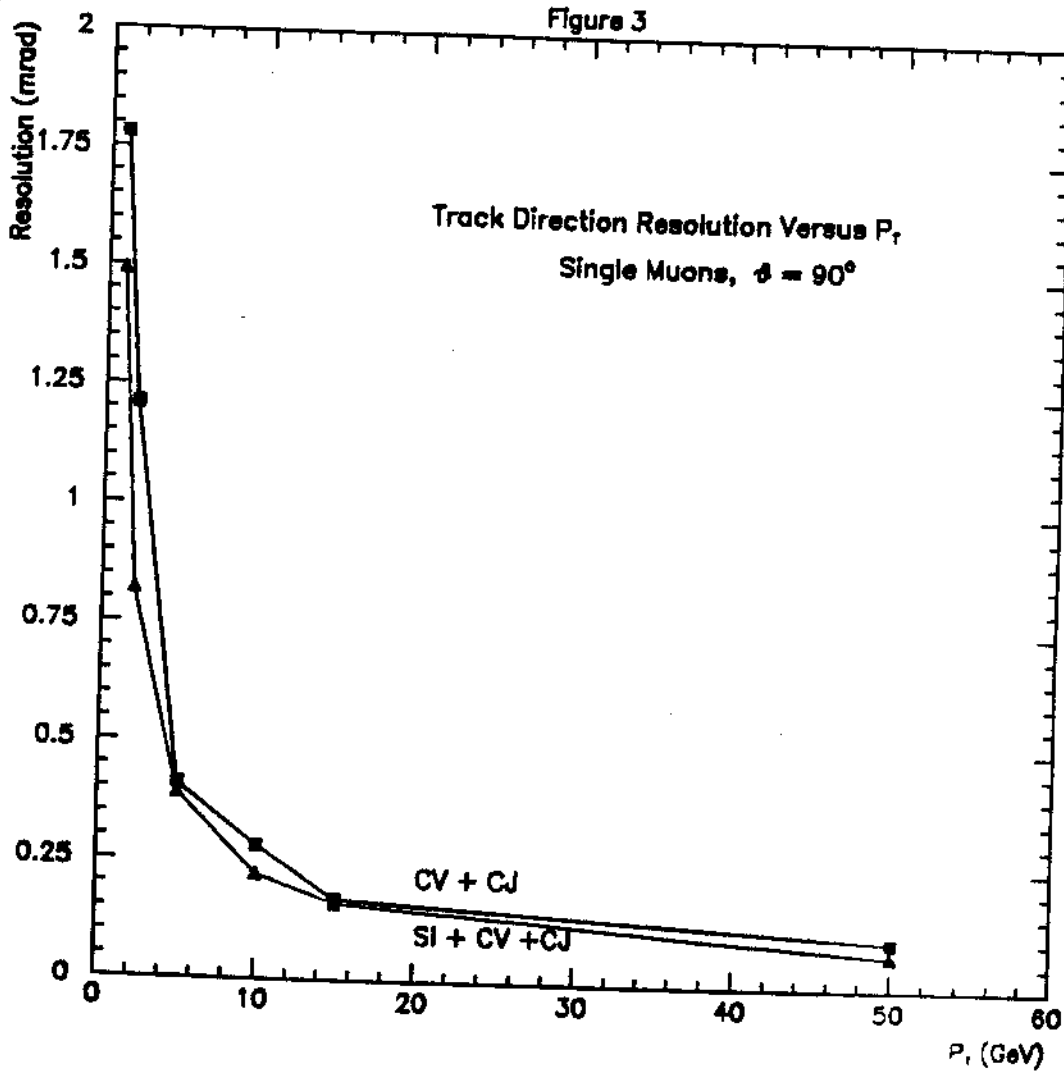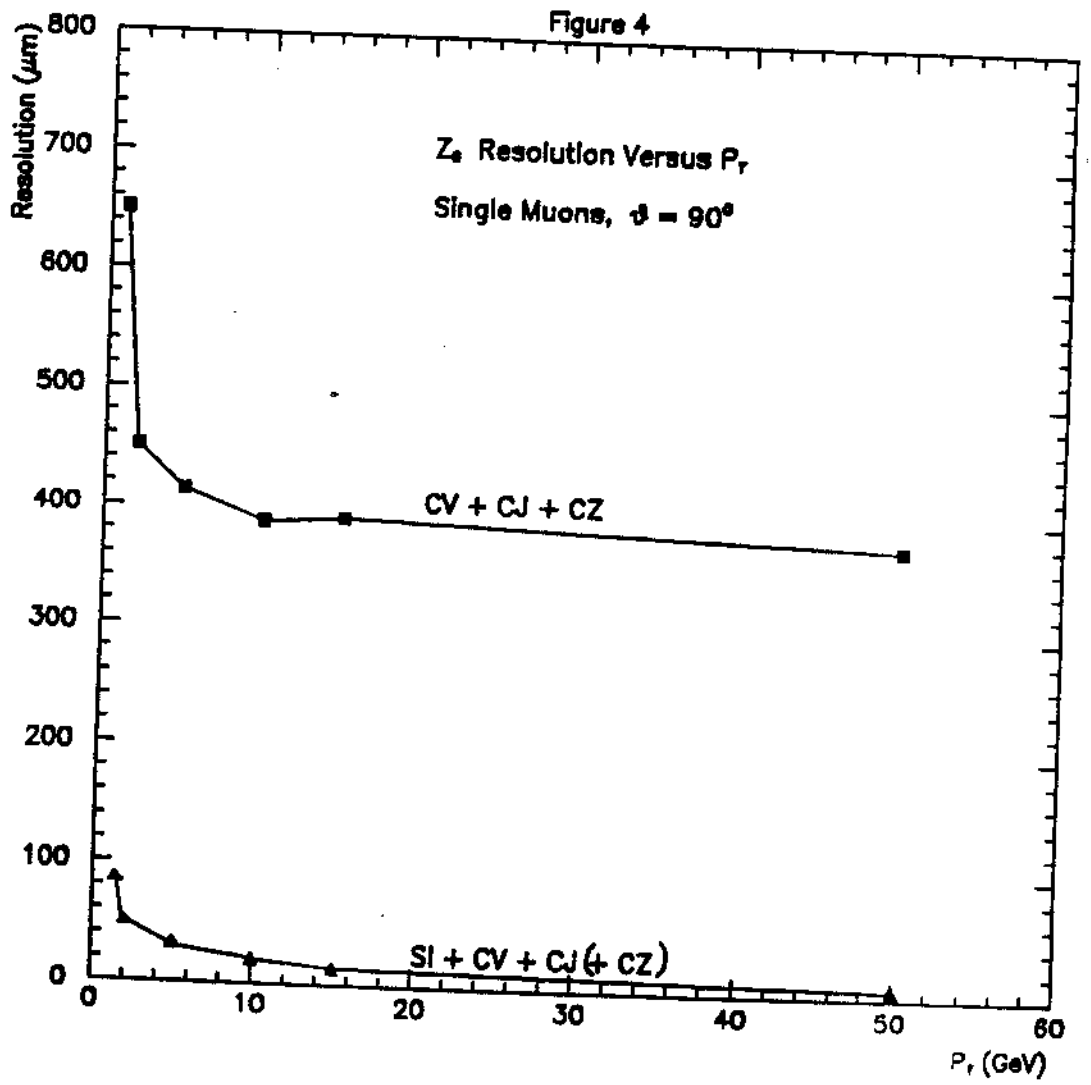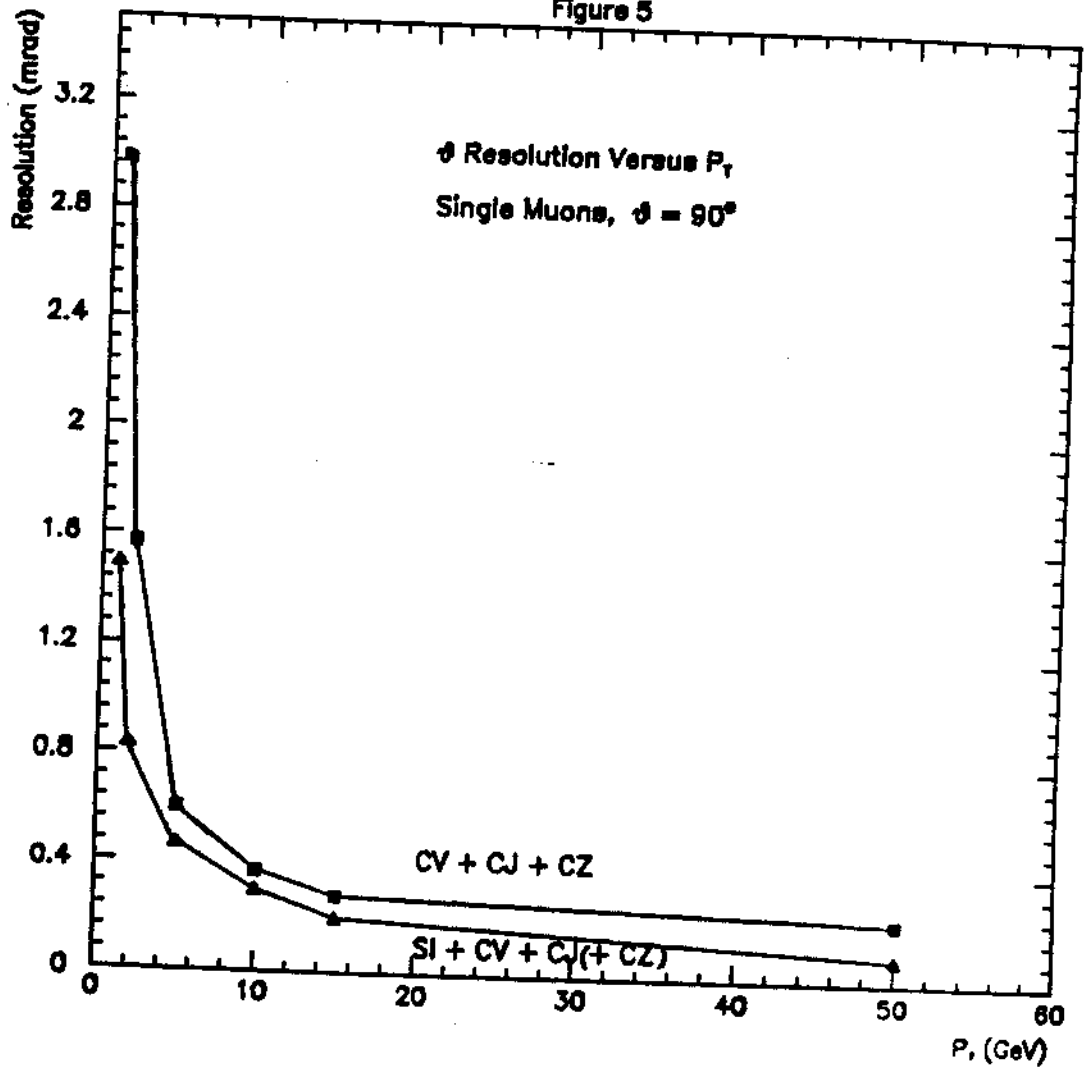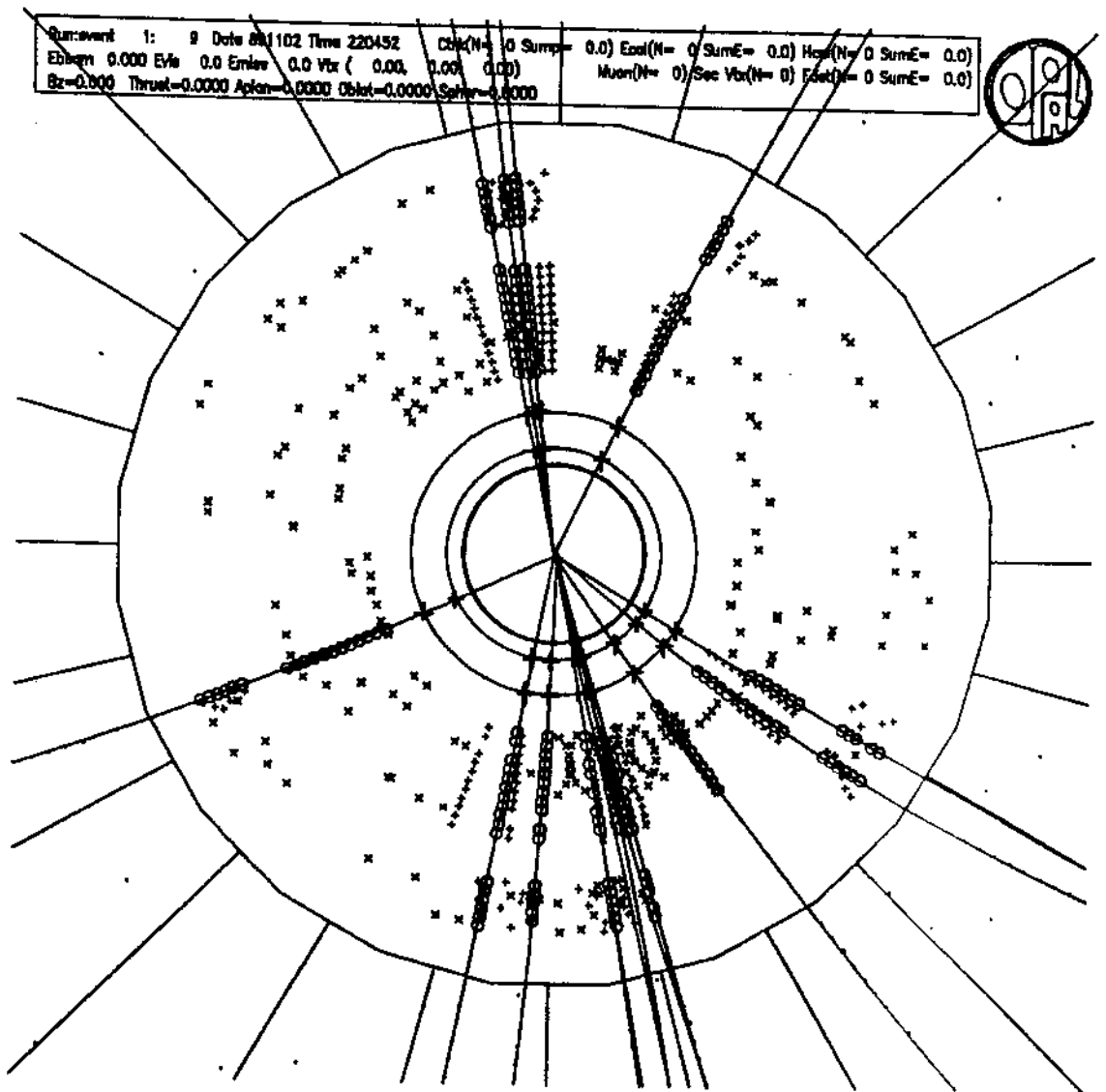
Figure 6

Monte Carlo $B\bar{B}$ event with noise hits in CV

Silicon hits are marked by crosses

Figure 7

Figure 8

ℓ(log(p)),extrap error dz (microns)). S1I

HBOOK   ID =   162   DATE 10/11/89

(b) dz vs log(p)

og(p)),extrap error ds (microns)). S1I

OOK   ID =   61   DATE 10/11/89

(a) ds vs log(p)
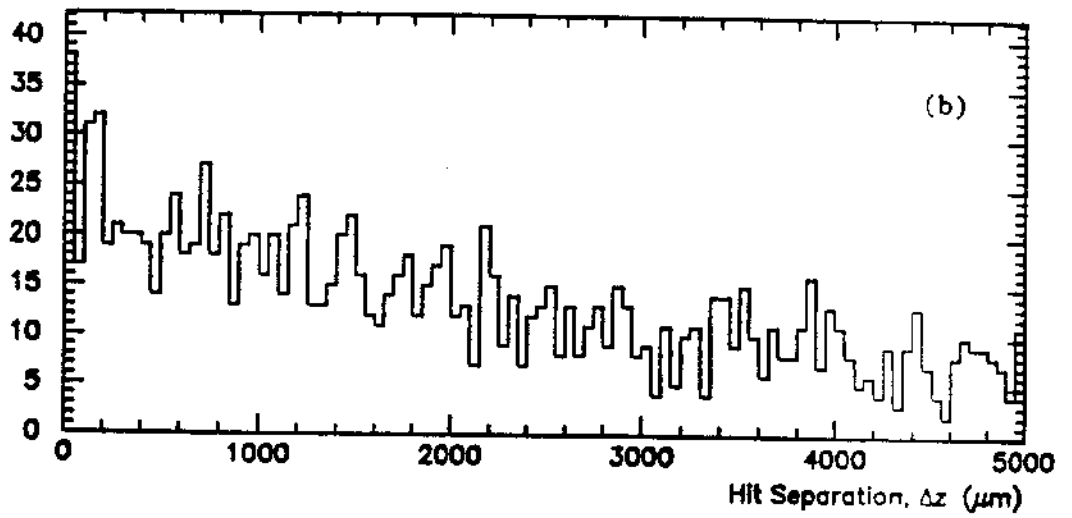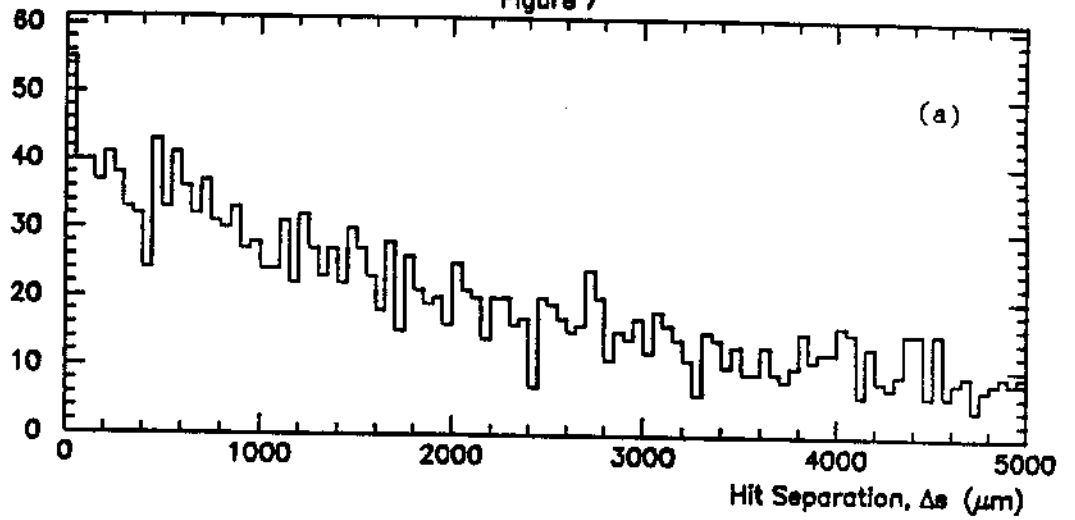
Figure 9
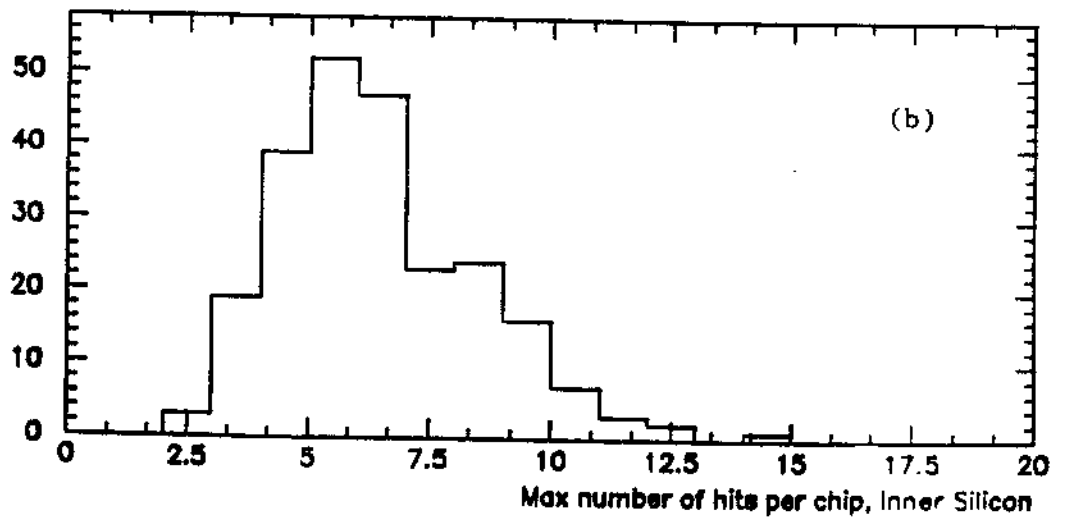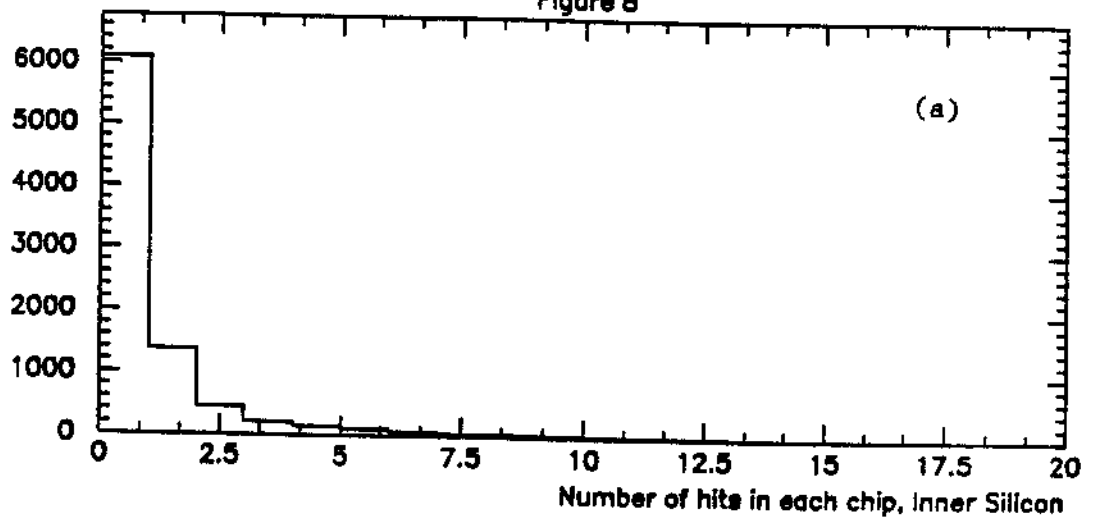
I(log(p)),extrap error dphi (microns/cm)), SI1

DATE 10/11/89

BOOK   ID =   62

ENTRIES = 4720
SATURATION AT= INFINITY
SCALE = +,2,3,...,A,B,...
STEP = MINIMUM=0

PLOT

STATISTICS

(a)

I(log(p)),extrap error dthela (microns/cm)), SI1

DATE 10/11/89

HBOOK   ID =   163

LOW-EDGE

ENTRIES = 4720
SATURATION AT= INFINITY
SCALE = +,2,3,...,A,B,...
STEP = MINIMUM=0

PLOT

STATISTICS

(b)

1Dist. ds. to true hit (SI1.SI2)

HBOOK   ID =   4

CHANNELS 10 U 0   DATE 10/11/89   NO = 2
          1 N 123456789012345678901234567890123456789012345678901234567890 V

```
          *************************************************************************
  OVE     *                                                                   *
 1450  .  *                                              +                   * *  OVE
 1400     *                                              +                 3 *     60
 1350     *                                                       +          *     59
 1300     *                                                       ++         *     58
 1250     *                                                     +   +      + *     57
 1200     *                                                        + +      *     56
 1150     *                               +                       ++ +    + *     55
 1100     *                                                   ++  33+    2 *     54
 1050     *                                                   + +          3 *     53
 1000     *                                                  +  +           *     52
  950     *                                               +22++           2 *     51
  900     *                                                22            +   *     50
  850     *                                             ++ +      +      +   *     49
  800     *                                          2+                  3 *     48
  750     *                                                          +     *     47
  700     *                                          ++     +            + *     46
  650     *                                     +  +32   +++         +     *     45
  600     *                                       +2++                 +   *     44
  550     *                                      35+                        *     43
  500     *                                     23+2                        *     42
  450     *                                    ++63                         *     41
  400     *                            +      2 +4+ ++    +                  *     40
  350     *                                  +36+ + +   +  + +              *     39
  300     *                                  654++ +2                       *     38
  250     *                                 238+2+3+ 22+                     *     37
  200     *                                 2AE4 4334+   +                   *     36
  150     *                                4DG855+2 +                        *     35
  100     *                        +     +8*YEA3+2 2                         *     34
   50     *                               3C**FG2+ +                         *     33
          *                              4****I54+ 2                         *     32
-  50     *                              +33L**Z93                           *     31
- 100     *                              +230V**G32                          *     30
- 150     *                         +    248****2                            *     29
- 200     *                              +22230Q**D2                         *     28
- 250     *                         +   23356AKU5                            *     27
- 300     *                          + +255384CJ2+ ++                        *     26
- 350     *                          +  +2++ E42                             *     25
- 400     *                        2 ++  ++8A+                               *     24
- 450     *                        +++  6+A3+                                *     23
- 500     *                         +  ++2384                                *     22
- 550     *                         +    244+                                *     21
- 600     *                 +       ++++62   +                               *     20
- 650     *                     +       32                                   *     19
- 700     *                 +         +52 +                                  *     18
- 750     *              +     +     ++++4    +                              *     17
- 800     *           +    +        2+                                       *     16
- 850     *                +        +2                                       *     15
- 900     *                       223                                        *     14
          *                 +     3                                          *     13
- 950     * +         +    2+2                                               *     13
-1000     * +             +3                                                 *     12
-1050     *         +     +2                                                 *     11
-1100     * 2           +                                                    *     10
-1150     *        ++   +                                                    *      9
-1200     * +     +2+    +                                                   *      8
-1250     *    + +                                                          *      7
-1300     * +  2 +                                                          *      6
-1350     *         +                                                        *      5
-1400     * 2                                                                *      4
-1450     * 2      +                                                         *      3
-1500     * 7              +                                                 *      2
  UND     * * +                                                              *      1
          *************************************************************************
LOW-EDGE  ---------------------------------------------------------------------
    1000    1111111111                                                1111111111
     100    5443322110099887766554433221      112233445566778899001122334 4
      10    05050505050505050505050505050505  505050505050505050505050505
      1.    0000000000000000000000000000000   000000000000000000000000000000
```

```
  *
  * ENTRIES =      4393                  PLOT          |   1   |   77
  * SATURATION AT=     INFINITY                  -------|-------|---------
  * SCALE  ..+.2.3.....A.B.            STATISTICS  17  | 4207  |   19
  * STEP =   1    * MINIMUM=0                    -------|-------|---------
                                                  71  |   1   |
```

Figure 11

ID1st, dz, to true hit (SI1.SI2)

HBOOK   ID =   6

CHANNELS 10 U 0   1   2   3   4   5   6 O
          1 N 12345678901234567890123456789012345678901234567890123456789 0 V
            ****

```
 OVE   *                                                              *  *  OVE
5800   *                                                         +2   *  *   60
5600   *                                                          5  4  *   59
5400   *                                                          5    3 *   58
5200   *                                                          62   +  *   57
5000   *                                                        +73  +  + *   56
4800   *                                                        42+  2  +  *   55
4600   *                                                       +83      +  *   55
4400   *                                                       52  ++      *   54
4200   *                                                      6+3+    +     *   53
4000   *                                                      62    +      *   52
3800   *                                                      8++   +      *   51
3600   *                                                   +  +632  3      *   50
3400   *                                                    +44  2          *   49
3200   *                                                    27422            *   48
3000   *                                                    32++             *   47
2800   *                                                   7932+             *   46
2600   *                                                   9632              *   45
2400   *                                                 +788  2+            *   44
2200   *                                                 A353    +           *   43
2000   *                                                +5272               *   42
1800   *                                              +  442+              *   41
1600   *                                              +9E72              *   40
1400   *                                             3AK43+              *   39
1200   *                                             +GP8+              *   38
1000   *                                            ++JT9              *   37
 800   *                                            3VV52             *   36
 600   *                                            ++*x3            *   35
 400   *                                           +3**42           *   34
 200   *                                          +  H**3++         *   33
- 200  *                                       +  +P**3            *   32
- 400  *                                 +            +***+        *   31
- 600  *                                           5****+          *   30
- 800  *                                           5**S  +         *   29
-1000  *                                        +  6**0            *   28
-1200  *                                         3**7+             *   27
-1400  *                                        +5**7   +          *   26
-1600  *                                         8Z*6              *   25
-1800  *                                        24SH6+             *   24
-2000  *                                        +4E04              *   23
-2200  *                                       ++6E82+             *   22
-2400  *                                      +259A  +             *   21
-2600  *                                       +280               *   20
-2800  *                                       +563   +           *   19
-3000  *                                     +  2582              *   18
-3200  *                                    ++4265+               *   17
-3400  *                                     2+59                 *   16
-3600  *                                    +44+6+                *   15
-3800  *                                     626+                 *   14
-4000  *                                   +22  6                 *   13
-4200  *                             +    ++  26                  *   12
-4400  *                             3    34                      *   11
-4600  *                             +  ++46+                     *   10
-4800  *                             ++  27                       *    9
-5000  *                            ++  45                        *    8
-5200  *                         +    25+                         *    7
-5400  *                              57                          *    6
-5600  *                         +++  39                          *    5
-5800  *                       *  +   2 +                         *    4
-6000  *                       * + +45+                           *    3
 UND   *                       *  +4                              *    2
       *                       * *  +                             *    1
```
            ****

LOW-EDGE   --
    1000   65555544444333332222211111   11111222223333344444555555
     100   08642086420864208642086420864 2   24680246802468024680246802468
      10   000000000000000000000000000000   000000000000000000000000000000
      1.   000000000000000000000000000000   000000000000000000000000000000
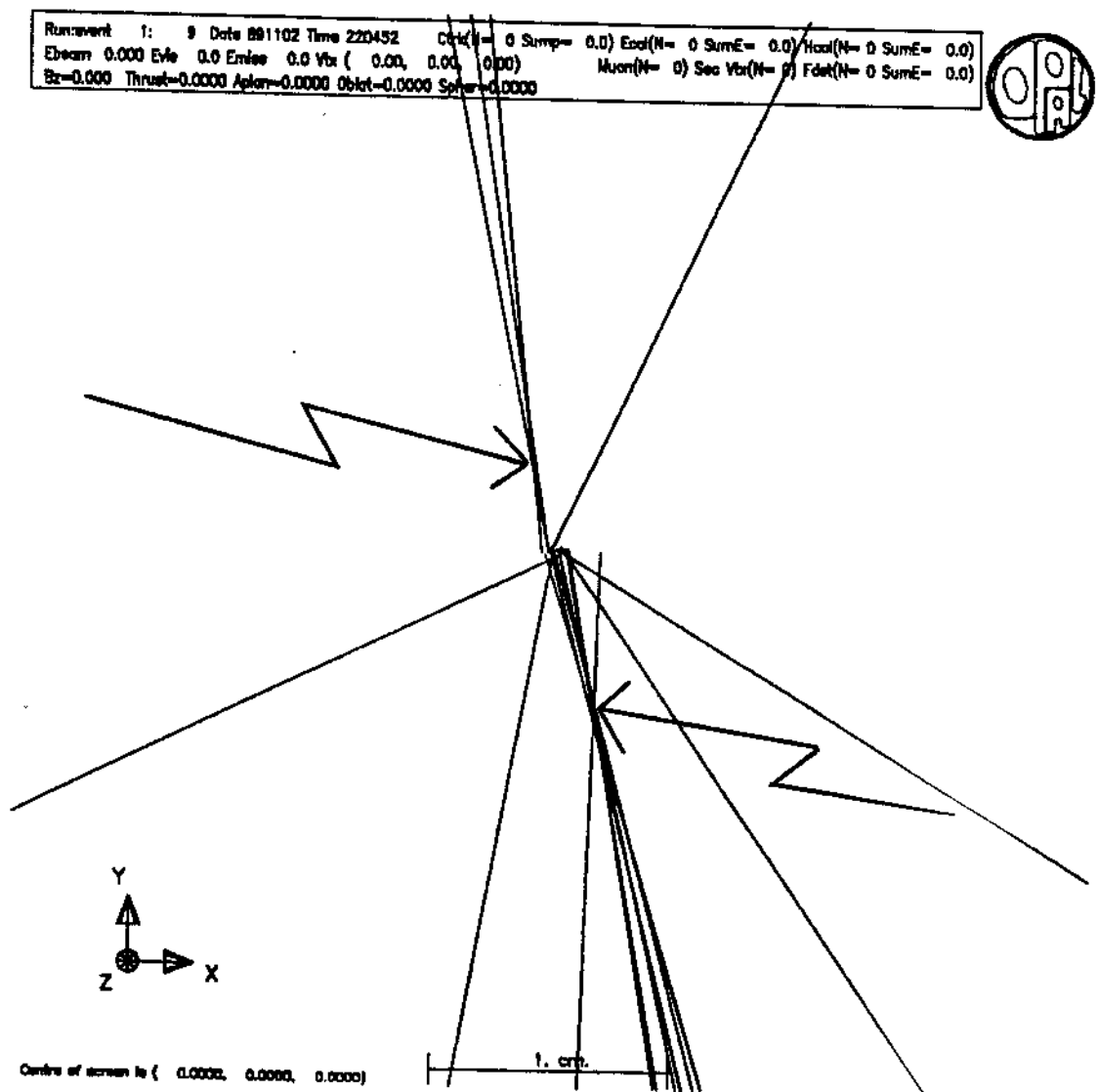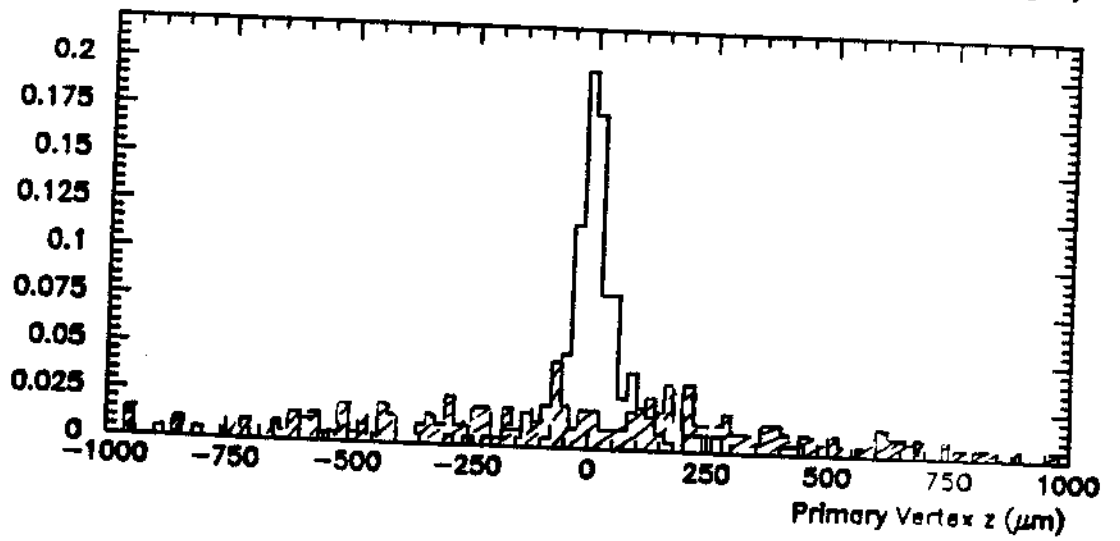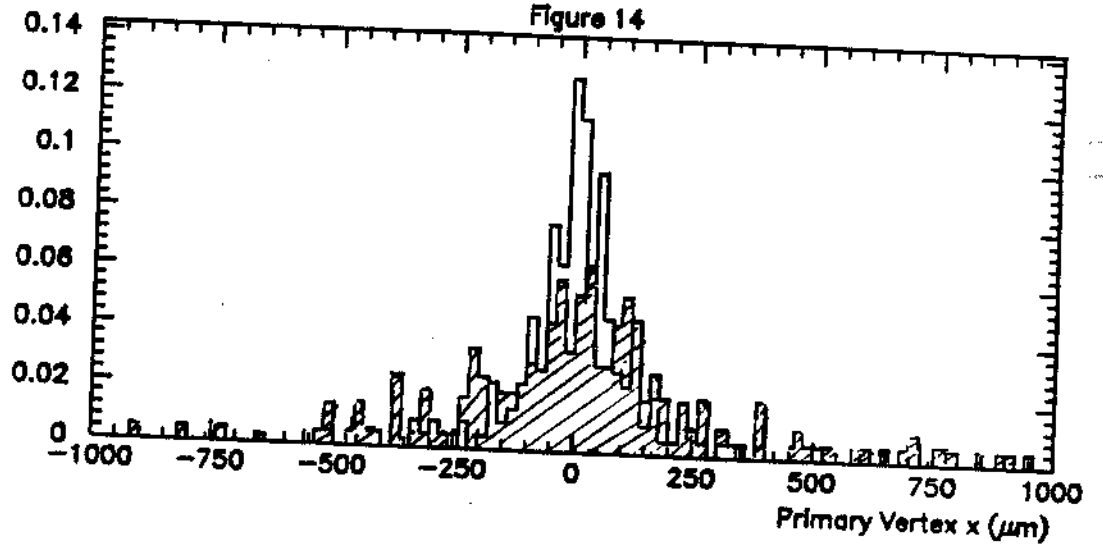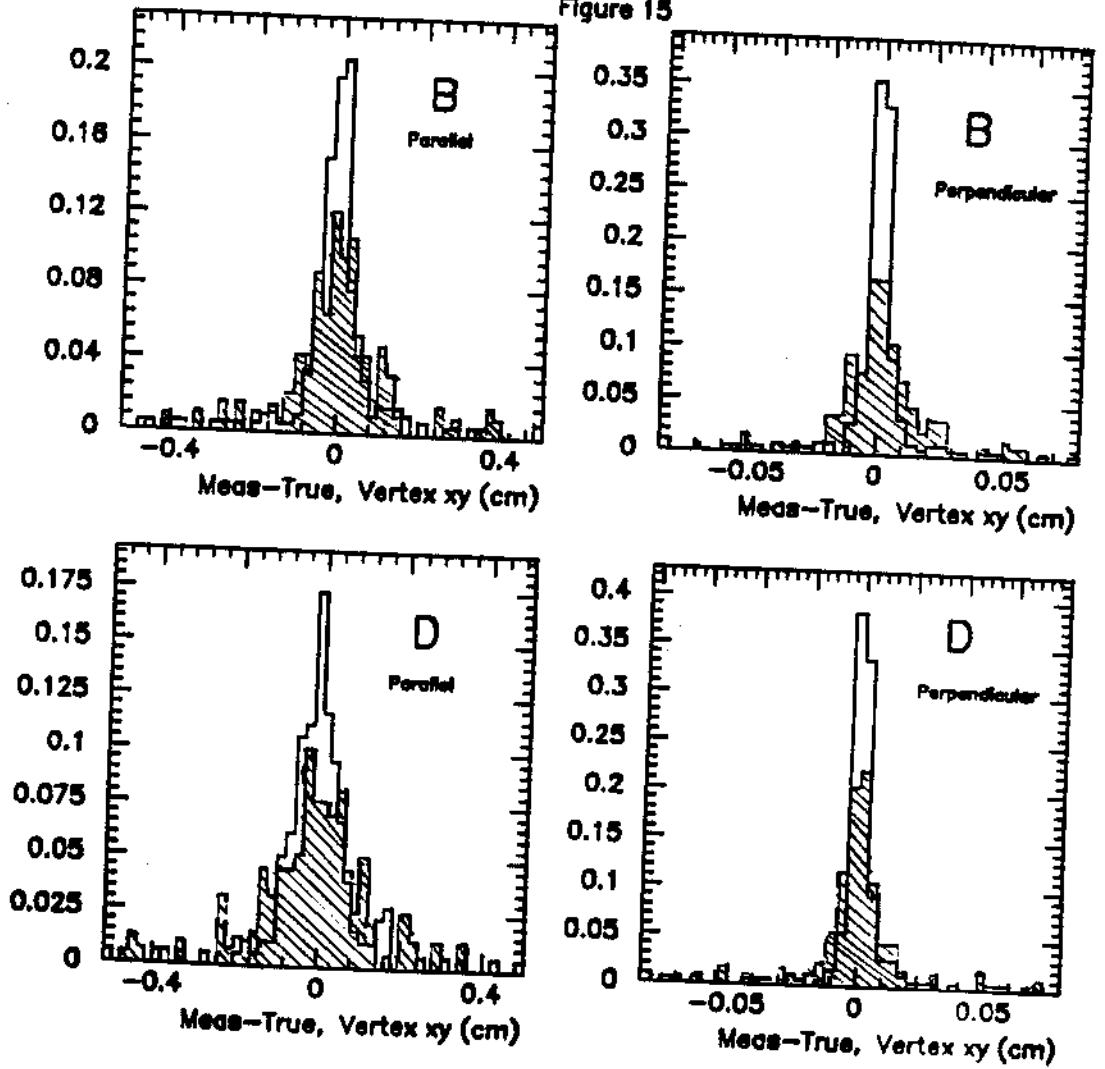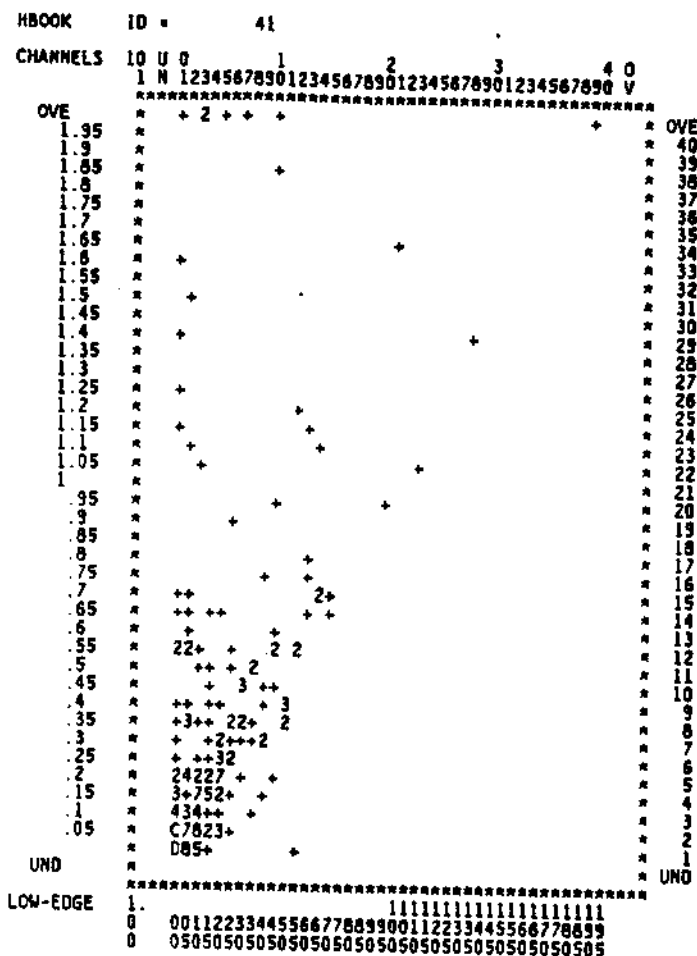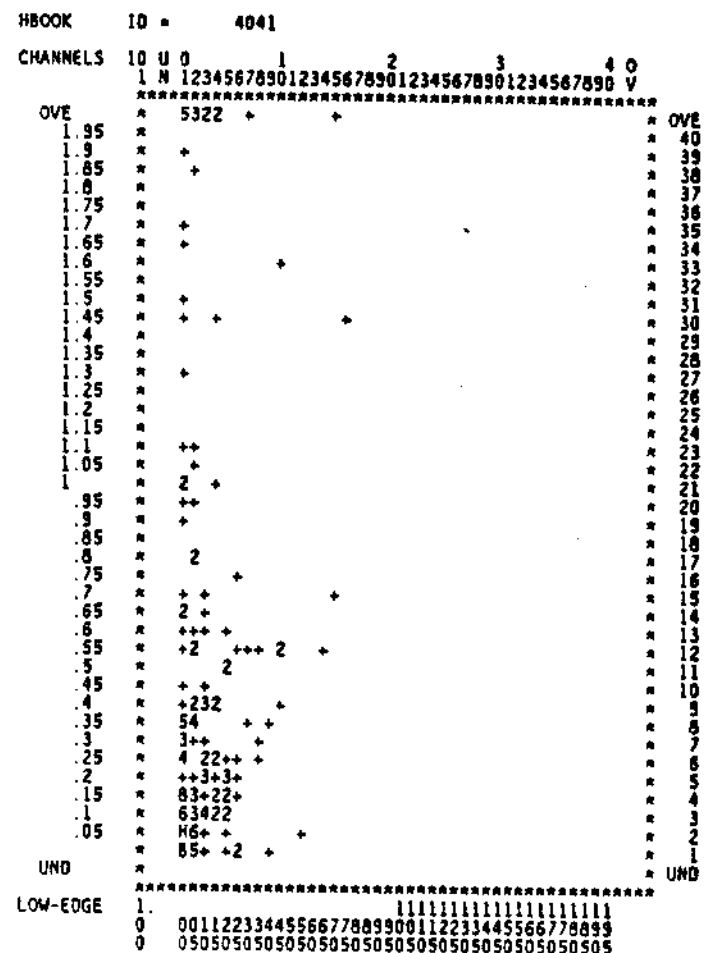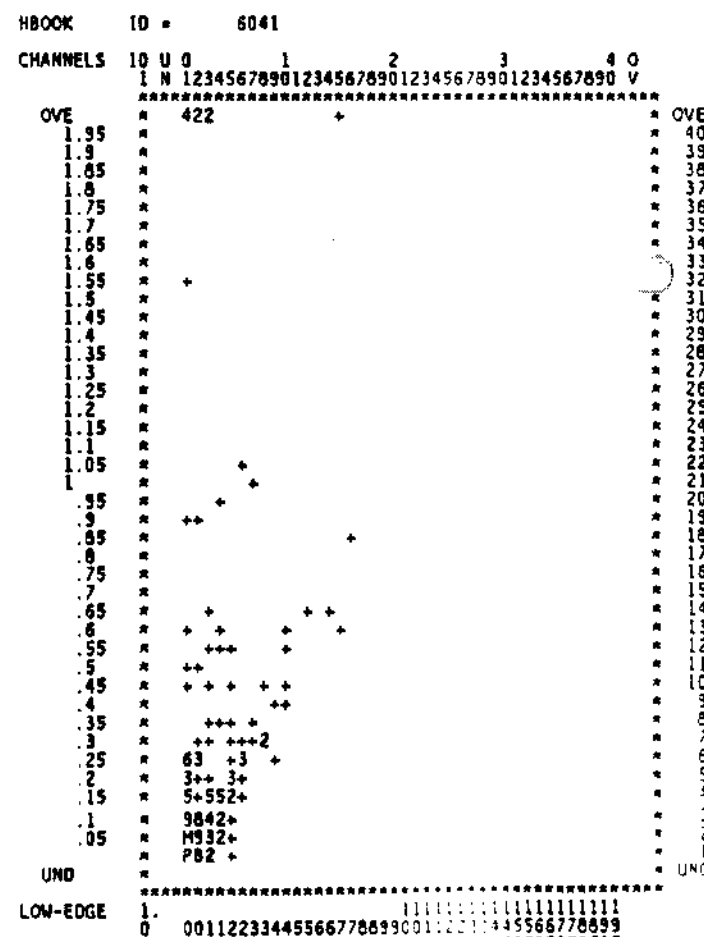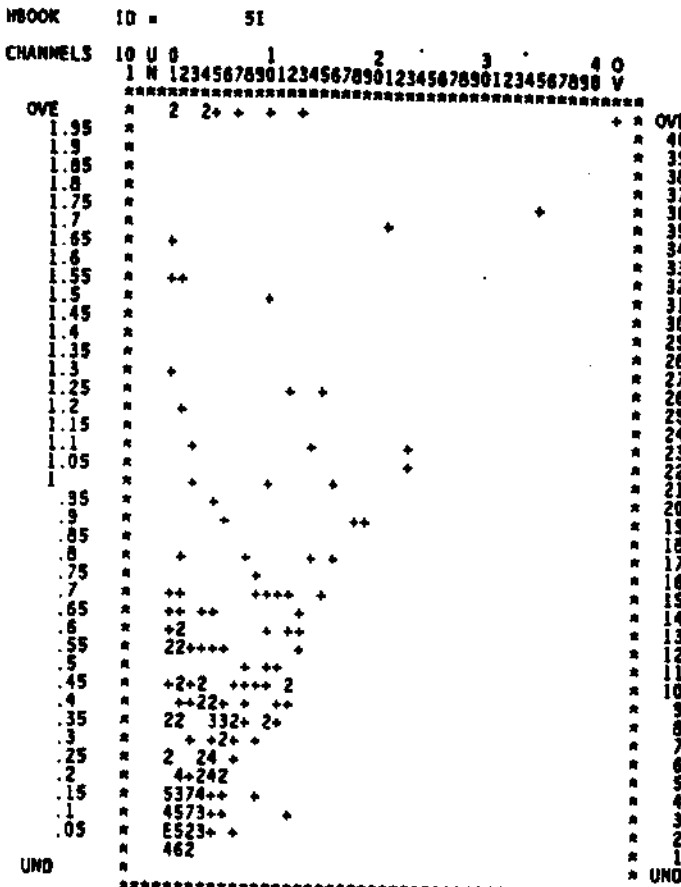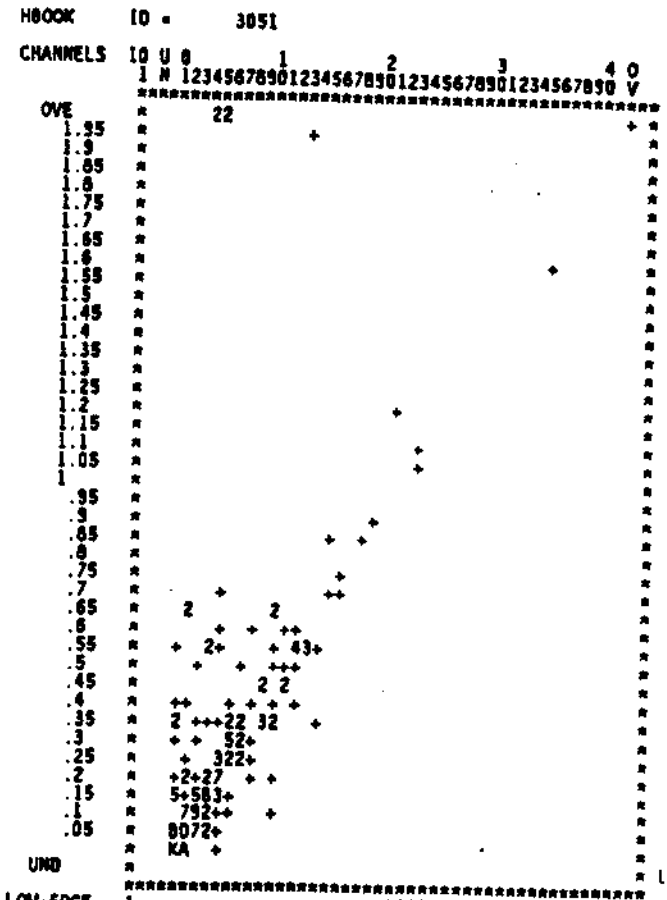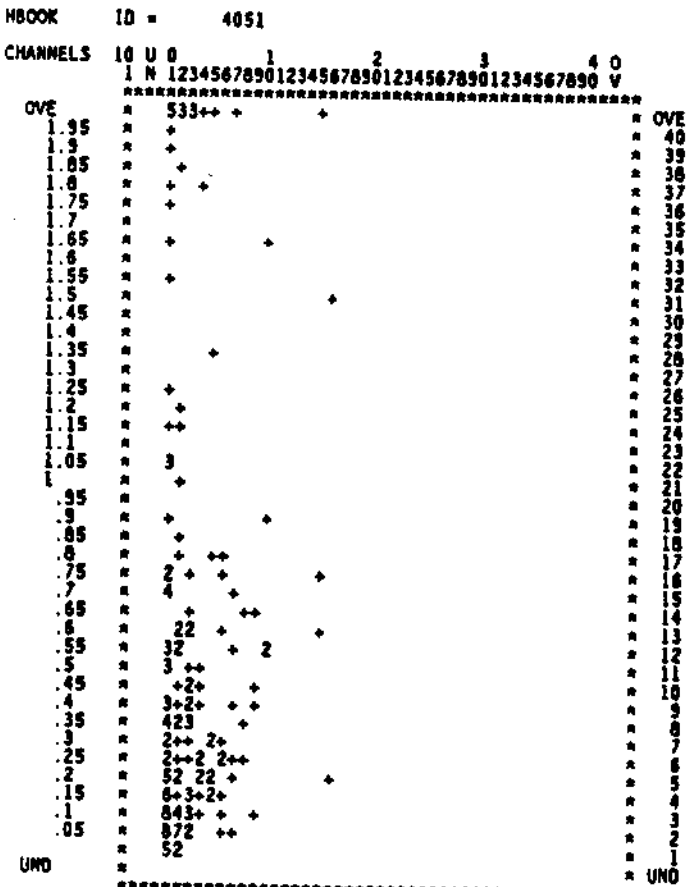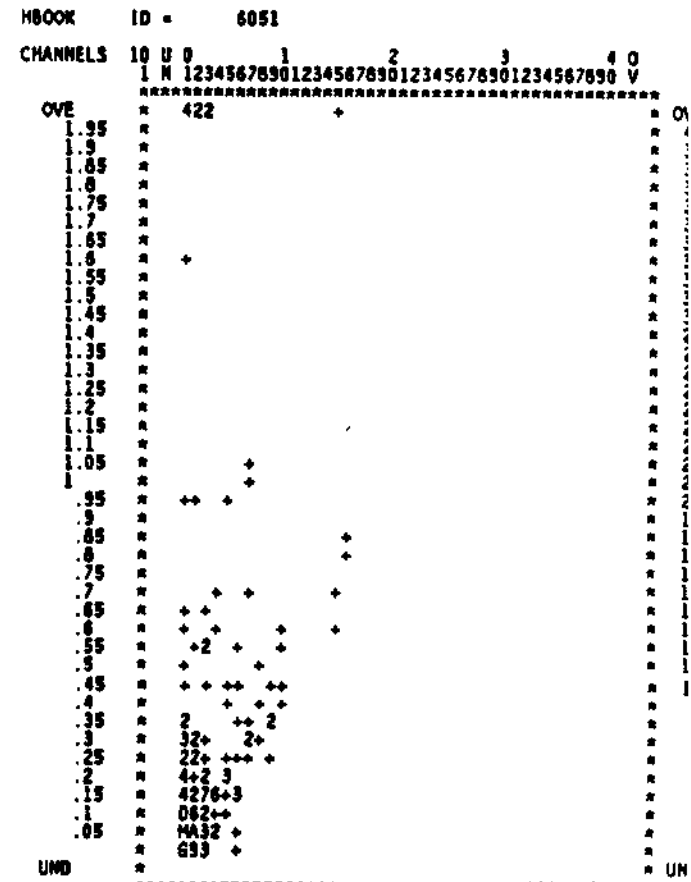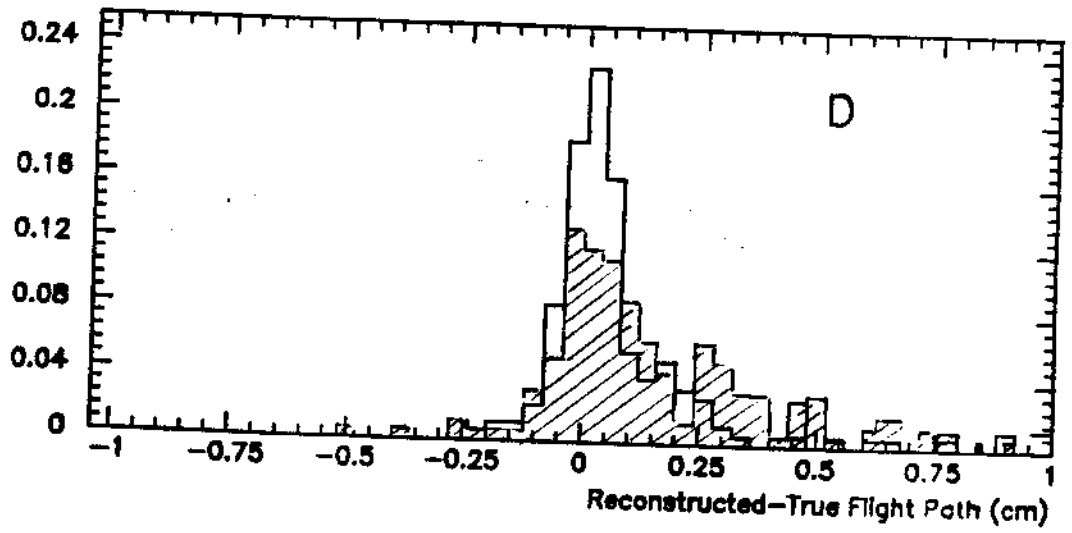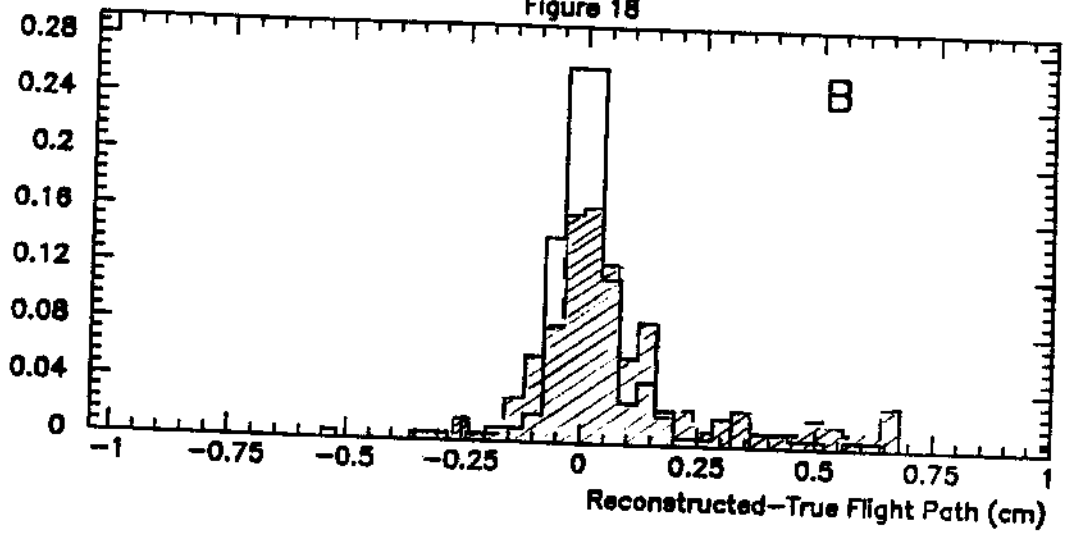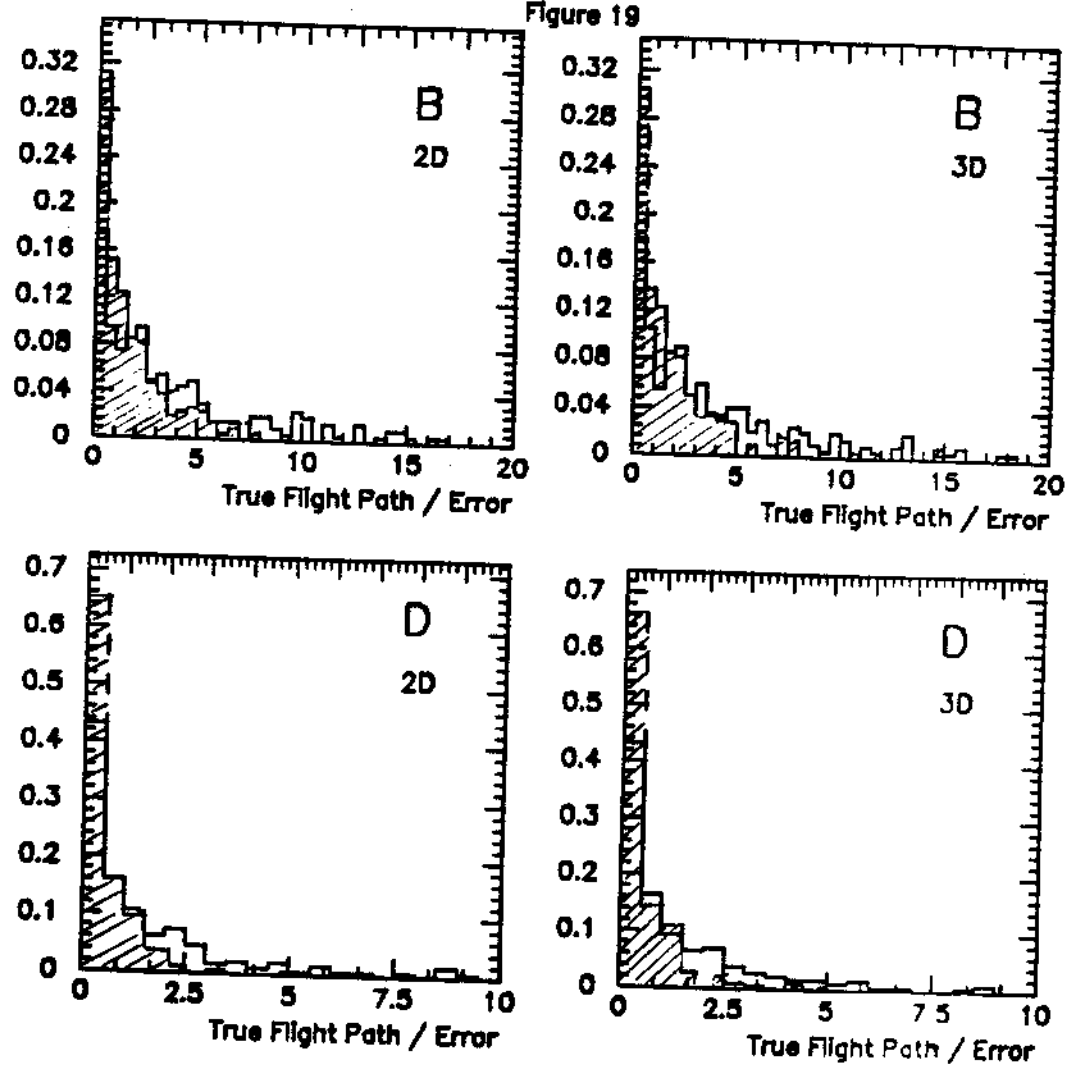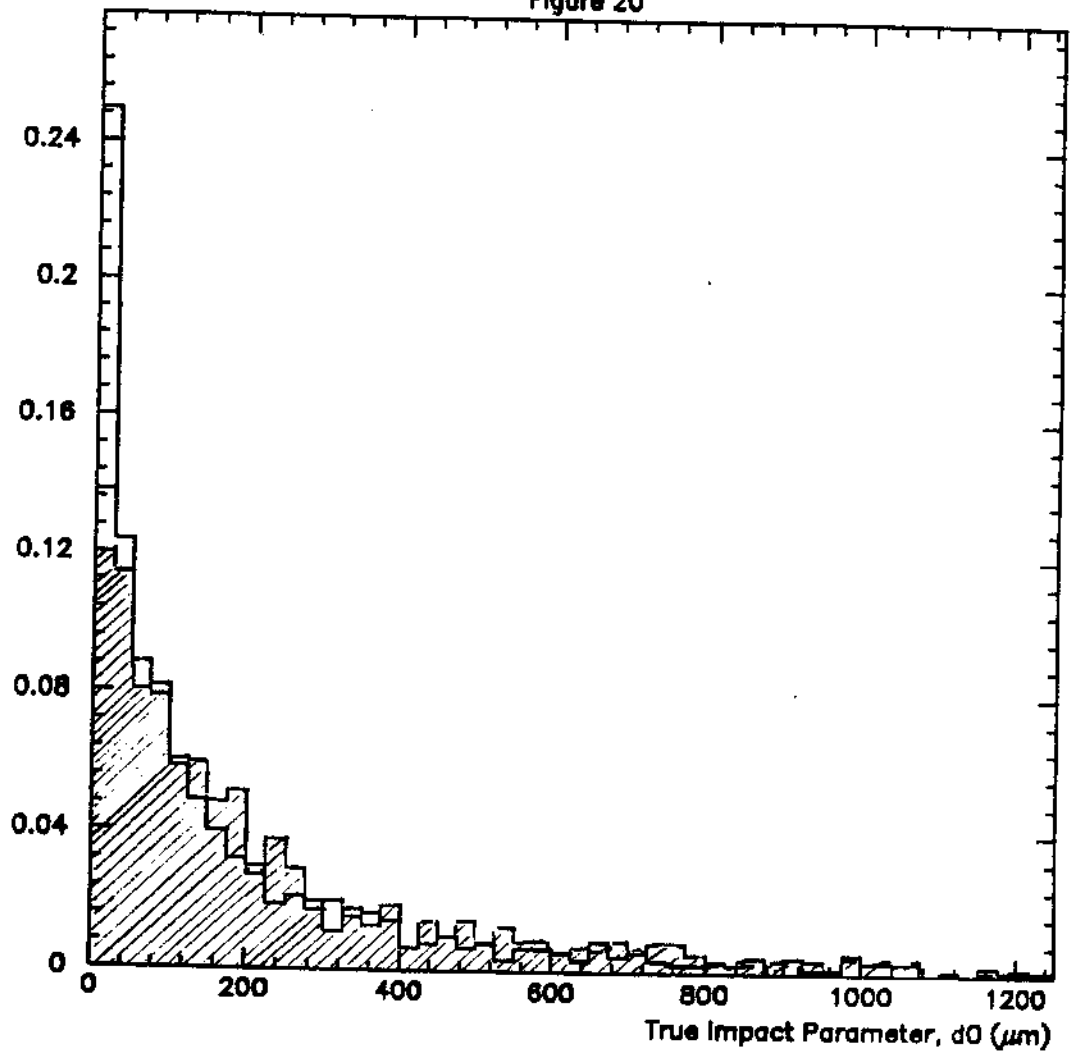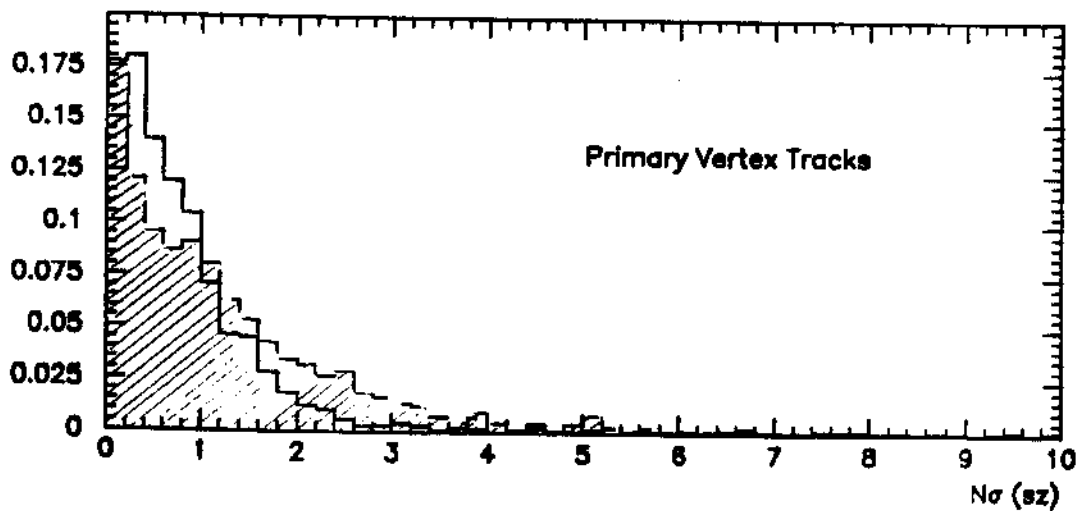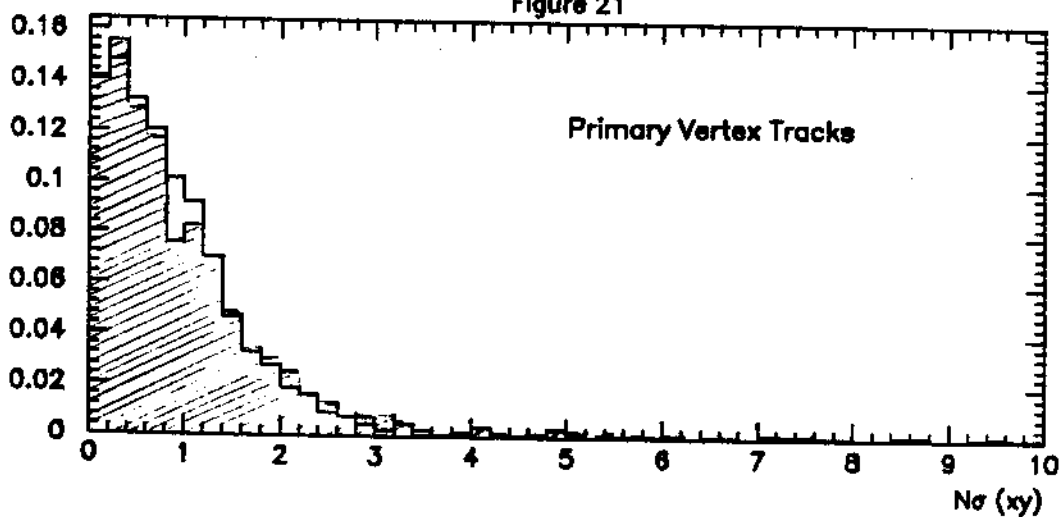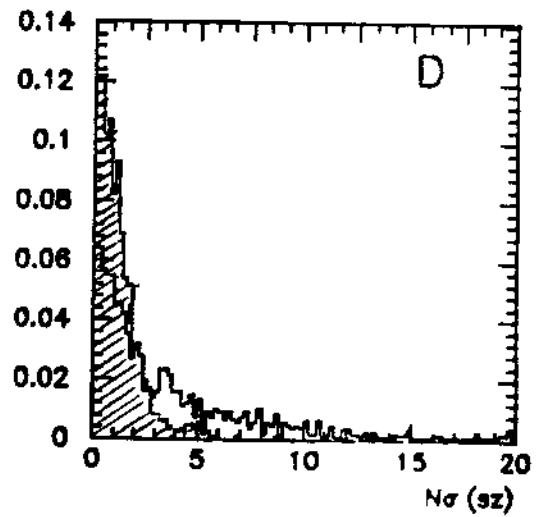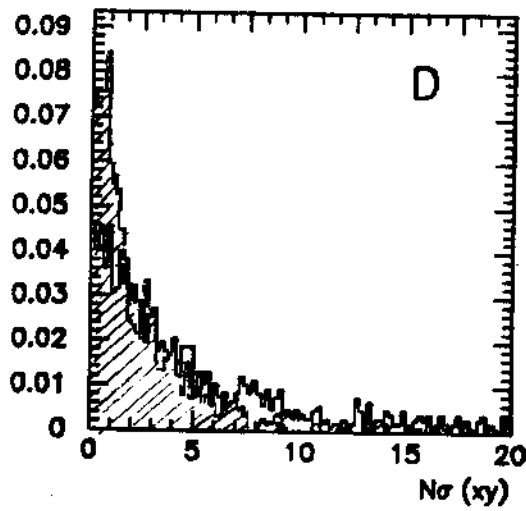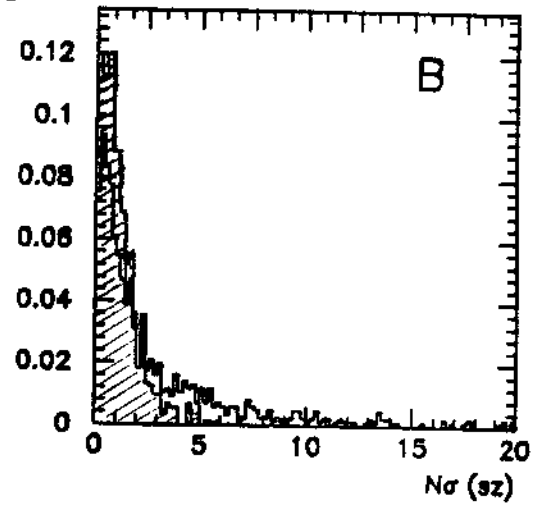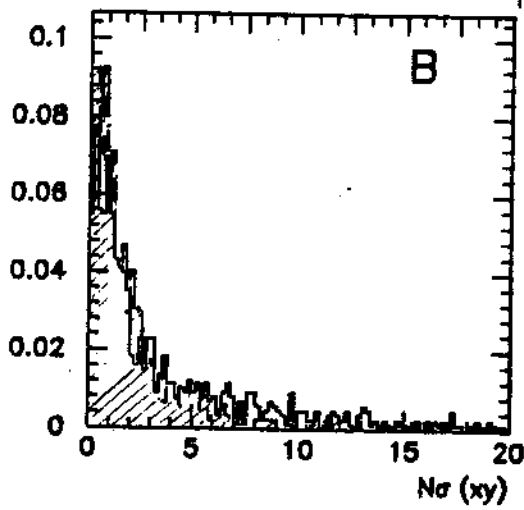
 *
 * ENTRIES =   4395
 * SATURATION AT=   INFINITY   PLOT   ------I---3---I--348---
 * SCALE ..+,2,3,....,A,B.   ------I-------I-------
 * STEP =   1   * MINIMUM=0   STATISTICS   ------2-I-3665-I--11---
                                                     ------I-------I-------
                                                      361 I   1   I
```

DATE 10/11/89                                    NO = 3

Figure 12

Figure 13

An expanded view of the vertex region of the event shown in fig 6

With the addition of the silicon hits the two decay vertices marked
by arrows can be identified.

Figure 14

Figure 15

120 8.0 flight path (true,meas)

HBOOK    ID =    41

(a)    B flight path without silicon

120 8.0 flight path (true,meas)

HBOOK    ID =    3041

(b)    B flight path with silicon

120 8.0 flight path (true,meas)

HBOOK    ID =    4041

(a)    D flight path without silicon

120 8.0 flight path (true,meas)

HBOOK    ID =    6041

(b)    D flight path with silicon

Figure 16

(a)    B flight path without silicon



(b)    B flight path with silicon



(a)    D flight path without silicon



(b)    D flight path with silicon

Figure 17

Figure 18



B

Reconstructed—True Flight Path (cm)

D

Reconstructed—True Flight Path (cm)

Figure 19



Top-left panel (B, 2D): y-axis values 0.32, 0.28, 0.24, 0.2, 0.16, 0.12, 0.08, 0.04, 0; x-axis 0, 5, 10, 15, 20; x-axis label: True Flight Path / Error

Top-right panel (B, 3D): y-axis values 0.32, 0.28, 0.24, 0.2, 0.16, 0.12, 0.08, 0.04, 0; x-axis 0, 5, 10, 15, 20; x-axis label: True Flight Path / Error

Bottom-left panel (D, 2D): y-axis values 0.7, 0.6, 0.5, 0.4, 0.3, 0.2, 0.1, 0; x-axis 0, 2.5, 5, 7.5, 10; x-axis label: True Flight Path / Error

Bottom-right panel (D, 3D): y-axis values 0.7, 0.6, 0.5, 0.4, 0.3, 0.2, 0.1, 0; x-axis 0, 2.5, 5, 7.5, 10; x-axis label: True Flight Path / Error

Figure 20

True Impact Parameter, d0 ($\mu$m)

Figure 21

Figure 22

**Appendix B**

# Secondary Vertex Finding for OPAL

M.F.Turner
Cambridge University

November 1989

## 1 Vertex Finding Process

The existing OPAL CX code was designed to find and fit the primary vertex, neutral V0 candidates and converted photons. Much of this code has been used and adapted to produce a more general vertex finding algorithm, with the intention of finding vertices of higher multiplicity. It is hoped that this will prove useful in the study of B-meson decays, particularly with the proposed silicon microvertex detector in OPAL. Some preliminary results are described here.

The analysis is based on a 2-d vertex fit which minimises the quantity $\chi^2_{r-\phi} = \sum D_i^2/\sigma_{D_i}^2$, for a set of tracks, where $D_i$ is the perpendicular distance (in $x$-$y$) from the vertex position to track $i$, and $\sigma_{D_i}$ is the error on this distance. The $z$ coordinate is calculated by taking a weighted average of the $z$ values for each track at the $(x,y)$ vertex. $z$ and its corresponding $\chi^2$ are given by the expressions $z = (\sum z_i/\sigma_{z_i}^2)/(\sum 1/\sigma_{z_i}^2)$ and $\chi_z^2 = \sum z_i^2/\sigma_{z_i}^2$, respectively, where $\sigma_{z_i}$ is the error on $z_i$.

Track parameters $(\kappa, d_0, \phi_0, \tan\lambda, z_0)$ and their errors for each reconstructed event are obtained from either the standard CT code or the silicon detector simulation code. A primary vertex is found using the CX routine CXPRIM, in which the 2-d fit is carried out on all tracks with $|d_0|$ less than a given value. Tracks with bad $\chi^2$ are removed and the vertex is refitted until each $\chi^2$ is below a specified cut, $\chi_p^2$.

Initially only those tracks which have not been fitted to the primary vertex are considered in the secondary vertex finding algorithm. They are looped over in order of increasing track parameter errors and the procedure summarised below is followed.

1. If any secondary vertices have already been found, the new track is added to the one for which the $\chi^2_{r-\phi}$ from a 2-d fit is a minimum, providing that cuts on both $\chi^2_{r-\phi}$ and $\chi_z^2$ are satisfied.

2. If the track cannot be fitted to any of the existing secondary vertices, intersections with previous tracks are found, using a method similar to that of V0 finding in the CX processor. Intersections are stored as candidate vertices if suitable constraints (on $\chi^2$ from vertex fit, direction of tracks, and so on) are satisfied.

After all candidate vertices have been found, an attempt is made to associate tracks originally fitted to the primary vertex with the secondary vertex candidates. At present there is no mechanism for identifying the better fit in these cases, so a track which is found to fit one of the secondaries will not be removed from the primary vertex. Another refinement of the algorithm involves iteration over a series of decreasing radii. Tracks belonging to vertices outside the given radius at one iteration are

eliminated from the next. This tends to reduce the number of incorrect vertices found close to the interaction point due to spurious intersections of tracks which have already been assigned to vertices. Only those secondary vertices with more than two associated tracks are currently retained.

## 2  B$\overline{\text{B}}$ events

100 B$\overline{\text{B}}$ events were generated using LUND 6.3 in the framework of GOPAL120. A simulation of the silicon microvertex detector was included, assuming double-sided ($r - \phi$ and $z$) readout for two silicon layers situated at radial positions of 6.5 and 7.5 cm between beam pipes at 6 and 8 cm. The existing OPAL detector was also fully simulated. Event reconstruction involved only the central detector processors in ROPE307 (CV, CJ, CZ, CT and CX). In the case of reconstruction with silicon, a pattern recognition algorithm was used to associate silicon hits to charged tracks by recognising alignment of the two hits with an existing track.

The vertex finding algorithm was applied, with and without silicon, to all events in the sample. In order to interpret the vertices after fitting, 'cheat word' information from the jet chamber event backs was used to identify the reconstructed tracks with those which were generated.

A primary vertex was found for every event, often containing tracks from secondary decays and interactions in addition to the true primary tracks. The entries in tables 1 and 2 refer to the number of events for which secondary vertices of the following types were reconstructed:

$B_n$  Containing only tracks from the $n^{th}$ B decay (n = 1 or 2)
$D_n$  Containing only tracks from the D originating from $B_n$
$B_n/D_n$  Containing tracks from $D_n$ or its parent $B_n$ and no others
$M_n$  Containing some tracks from $B_n$ or $D_n$ and some others
$M$  Containing no tracks from the B or D decays

There can be some overlap within events when several vertices containing different subsets of tracks from the same decay are found. This aspect was considered in the calculation of purities and efficiencies, where it was assumed that classification of the vertices into two sets (those from the $B_1$ or $D_1$ decays and those from the $B_2$ or $D_2$ decays) would be possible without the help of cheat information. Tables 3 and 4 summarise the reconstruction efficiencies and purities which were calculated using

$$\text{Efficiency} = \frac{\text{No. of vertices including } some \text{ B and/or D tracks from a particular B decay}}{\text{Total no. of B vertices generated}}$$

$$\text{Purity} = \frac{\text{No. of vertices containing } only \text{ B and/or D tracks from a particular B decay}}{\text{Total no. of vertices found}}$$

## 3  u$\overline{\text{u}}$ events

The algorithm was also run on 100 u$\overline{\text{u}}$ events with a single set of $\chi^2$ cuts ($\chi_p^2 = 10.0$, $\chi_{s,r-\phi}^2 = 2.0$, $\chi_{s,z}^2 = 5.0$). These events were generated with two layers of silicon at radii of 6 and 8 cm and a single beampipe at 5 cm. Results obtained for an equivalent sample of B$\overline{\text{B}}$ events in this configuration were found to be consistent with those described above. Only one secondary vertex was found within 1 cm of the primary vertex position when the u$\overline{\text{u}}$ events were reconstructed with silicon, and only two were found without silicon. These results are very encouraging, and other quark types should now be studied.

# 4  Summary of results

It can be seen from tables 1 and 2 that the number of 'mixed' secondary vertices, containing some B or D tracks, is roughly the same both with and without silicon. However, the number of vertices containing only tracks from the B or D decays is, on average, a factor of 7 higher in the case of reconstruction with silicon than without. As would be expected, there are considerably more spurious vertices, containing no B or D tracks, when there is no silicon detector present.

Individual values of purity and efficiency are relatively insensitive to cuts on $\chi^2_{r-\phi}$ and $\chi^2_z$ imposed on the secondary vertex fit. It was found that decreasing the $\chi^2$ cut on the primary vertex had the effect of increasing the efficiency by freeing some of the secondary decay tracks. At the same time the number of primary vertex tracks correctly assigned to that vertex was reduced, leading to a less pure sample of secondary vertices.

The average values of purity and efficiency for secondary vertex finding with silicon are 86% and 27% respectively, in contrast to the corresponding values of 32% and 10% without silicon. This represents a factor of 2-3 improvement in both quantities, showing that a geometrical vertex finding procedure could be of considerable use for B physics studies with a silicon microvertex detector in OPAL.

Table 1: Summary of secondary vertices found with silicon for 100 $B\bar{B}$ events

| $\chi^2$ cuts | | | 1$^{st}$ B decay | | | | 2$^{nd}$ B decay | | | | Other |
|---|---|---|---|---|---|---|---|---|---|---|---|
| $\chi^2_p$ | $\chi^2_{s,r-\phi}$ | $\chi^2_{s,z}$ | $B_1$ | $D_1$ | $B_1/D_1$ | $M_1$ | $B_2$ | $D_2$ | $B_2/D_2$ | $M_2$ | M |
| 10 | 2 | 5 | 2 | 6 | 20 | 11 | 4 | 2 | 18 | 3 | 0 |
| 10 | 2 | 2 | 3 | 6 | 17 | 7 | 4 | 7 | 17 | 2 | 0 |
| 10 | 3 | 3 | 3 | 7 | 20 | 10 | 3 | 6 | 17 | 3 | 0 |
| 10 | 1 | 1 | 3 | 8 | 8 | 5 | 3 | 7 | 11 | 0 | 0 |
| 10 | 5 | 5 | 1 | 6 | 22 | 13 | 3 | 7 | 19 | 4 | 0 |
| 10 | 10 | 10 | 2 | 7 | 23 | 15 | 3 | 5 | 19 | 9 | 0 |
| 10 | 3 | 5 | 2 | 7 | 23 | 11 | 3 | 7 | 19 | 4 | 0 |
| 10 | 1 | 2 | 3 | 8 | 14 | 6 | 3 | 7 | 15 | 2 | 0 |
| 5 | 2 | 2 | 2 | 8 | 20 | 10 | 6 | 8 | 16 | 3 | 0 |
| 2 | 2 | 2 | 7 | 14 | 29 | 20 | 5 | 7 | 20 | 13 | 1 |

Table 2: Summary of secondary vertices found without silicon for 100 $B\bar{B}$ events

| $\chi^2$ cuts | | | 1$^{st}$ B decay | | | | 2$^{nd}$ B decay | | | | Other |
|---|---|---|---|---|---|---|---|---|---|---|---|
| $\chi^2_p$ | $\chi^2_{s,r-\phi}$ | $\chi^2_{s,z}$ | $B_1$ | $D_1$ | $B_1/D_1$ | $M_1$ | $B_2$ | $D_2$ | $B_2/D_2$ | $M_2$ | M |
| 10 | 2 | 5 | 1 | 0 | 4 | 10 | 1 | 0 | 4 | 4 | 2 |
| 10 | 2 | 2 | 0 | 0 | 2 | 7 | 0 | 0 | 3 | 2 | 1 |
| 10 | 3 | 3 | 0 | 0 | 5 | 9 | 1 | 0 | 2 | 3 | 1 |
| 10 | 1 | 1 | 0 | 0 | 1 | 4 | 0 | 0 | 3 | 1 | 2 |
| 10 | 5 | 5 | 2 | 0 | 4 | 12 | 2 | 0 | 2 | 7 | 3 |
| 10 | 10 | 10 | 1 | 0 | 5 | 17 | 2 | 0 | 3 | 10 | 3 |
| 10 | 3 | 5 | 1 | 0 | 5 | 10 | 1 | 0 | 2 | 6 | 3 |
| 10 | 1 | 2 | 0 | 0 | 0 | 8 | 0 | 0 | 3 | 2 | 2 |
| 5 | 2 | 2 | 1 | 1 | 4 | 8 | 0 | 1 | 5 | 3 | 5 |
| 2 | 2 | 2 | 1 | 1 | 5 | 16 | 1 | 0 | 3 | 7 | 8 |

4

Table 3: Efficiencies and purities for secondary vertex finding with silicon

| $\chi^2_p$ cut | $\chi^2_{s,r-\phi}$ cut | $\chi^2_{s,z}$ cut | Purity | Efficiency |
|---|---|---|---|---|
| 10 | 2 | 5 | 87% | 30% |
| 10 | 2 | 2 | 87% | 26% |
| 10 | 3 | 3 | 89% | 27% |
| 10 | 1 | 1 | 92% | 20% |
| 10 | 5 | 5 | 87% | 30% |
| 10 | 10 | 10 | 76% | 33% |
| 10 | 3 | 5 | 88% | 30% |
| 10 | 1 | 2 | 92% | 24% |
| 5 | 2 | 2 | 85% | 33% |
| 2 | 2 | 2 | 80% | 44% |

Table 4: Efficiencies and purities for secondary vertex finding without silicon

| $\chi^2_p$ cut | $\chi^2_{s,r-\phi}$ cut | $\chi^2_{s,z}$ cut | Purity | Efficiency |
|---|---|---|---|---|
| 10 | 2 | 5 | 42% | 11% |
| 10 | 2 | 2 | 29% | 6% |
| 10 | 3 | 3 | 35% | 9% |
| 10 | 1 | 1 | 36% | 4% |
| 10 | 5 | 5 | 30% | 13% |
| 10 | 10 | 10 | 29% | 17% |
| 10 | 3 | 5 | 35% | 11% |
| 10 | 1 | 2 | 20% | 6% |
| 5 | 2 | 2 | 40% | 10% |
| 2 | 2 | 2 | 26% | 15% |